Lamina-scale diagenetic mass transfer in lacustrine organic-rich shales and impacts on shale oil reservoir formation

Yingchang Cao, Kelai Xi, Xiaobing Niu, Miruo Lin, Weijiao Ma, Zehan Zhang, and Helge Hellevang

ABSTRACT

Lacustrine organic-rich shales have recently become important petroleum exploration targets. Adequate reservoir characterization is vital for determining the potential for shale oil exploration and development. Fluid–rock interaction and diagenetic mass transfer in organic-rich shales are essential processes during shale oil reservoir formation. Based on detailed petrographic investigation, in situ element and isotope measurement, and organic geochemistry analysis, diagenetic mass transfers and related organic–inorganic interactions were investigated using a suite of organic-rich shales from the Triassic Yanchang Formation of the Ordos Basin. Organic-rich shales consist of silt-sized felsic laminae and organic-rich laminae. Silt-sized felsic laminae are dominated mainly by K-feldspar, whereas illite is the most abundant mineral in organic-rich laminae. Authigenic quartz and euhedral pyrite are the major diagenetic minerals in organic-rich laminae, whereas K-feldspar dissolution occurs extensively in silt-sized felsic laminae. Smectite-to-illite conversion has played a significant role in the diagenetic alteration of organic-rich shales. This reaction not only induced overpressure to generate microfractures for authigenic quartz growth but it also provided the required silica source for authigenic quartz precipitation. Petrographic and geochemical evidence indicates that organic acids generated in organic-rich laminae have migrated to silt-sized felsic laminae, and K^+ and aqueous SiO_2 yielded from K-feldspar dissolution in silt-sized felsic laminae have been transported to organic-rich laminae. Based on organic–inorganic interactions related to authigenic quartz formation, we conclude that the lamina-scale open diagenetic system allows mass transfer to

Manuscript received February 7, 2023; provisional acceptance June 6, 2023; revised manuscript received July 6, 2023; revised manuscript provisional acceptance July 25, 2023; 2nd revised manuscript received August 24, 2023; final acceptance October 5, 2023; preliminary ahead of print version published December 18, 2023.
DOI:10.1306/12212323018

AUTHORS

YINGCHANG CAO ~ *National Key Laboratory of Deep Oil and Gas, China University of Petroleum (East China), Qingdao, Shandong, China; caoych@upc.edu.cn*

Yingchang Cao is a professor at China University of Petroleum (East China). His research interests lie in the fields of sequence stratigraphy, sedimentology, and conventional and unconventional oil reservoir formation. He is a corresponding author of this paper.

KELAI XI ~ *National Key Laboratory of Deep Oil and Gas, China University of Petroleum (East China), Qingdao, Shandong, China; xikelai@upc.edu.cn*

Kelai Xi is a professor at China University of Petroleum (East China). His research focuses on tight sandstone diagenesis, reservoir quality prediction, and shale oil reservoir characterization. He is a corresponding author of this paper.

XIAOBING NIU ~ *National Key Laboratory of Deep Oil and Gas, China University of Petroleum (East China), Qingdao, Shandong, China; PetroChina Changqing Oilfield Company, Xi'an Shaanxi, China; nxb_cq@petrochina.com.cn*

Xiaobing Niu is a professor at PetroChina Changqing Oilfield Company. His research interests lie in unconventional oil and gas reservoir characterization as well as exploration management.

MIRUO LIN ~ *National Key Laboratory of Deep Oil and Gas, China University of Petroleum (East China), Qingdao, Shandong, China; 1152823158@qq.com*

Miruo Lin is a Ph.D. student at China University of Petroleum (East China). Her research interests lie in unconventional reservoir characterization and shale oil formation.

WEIJIAO MA ~ *National Key Laboratory of Deep Oil and Gas, China University of Petroleum (East China), Qingdao, Shandong, China; weijiao.ma@upc.edu.cn*

Weijiao Ma received her Ph.D. from Beijing University and is a postdoctoral research fellow at China University of Petroleum (East China). Her research interests lie in organic geochemistry and shale oil formation.

ZEHAN ZHANG ~ *National Key Laboratory of Deep Oil and Gas, China University of Petroleum (East China), Qingdao, Shandong, China; zzhydns@163.com*

Zehan Zhang is a master's degree student at China University of Petroleum (East China). Her research interests lie in unconventional oil and gas reservoir characterization.

HELGE HELLEVANG ~ *Department of Geosciences, University of Oslo, Blindern Oslo, Norway; helge.hellevang@geo.uio.no*

Helge Hellevang is a professor at the University of Oslo. His research interests lie in the fields of reservoir diagenesis and low-temperature geochemistry.

ACKNOWLEDGMENTS

The research was cofunded by the Innovation Research Group of the Natural Fund Committee (Grant No. 41821002), the National Natural Science Foundation of China (Grant No. 42072161), the Taishan Scholars Program (tsqn202301625), and the Fundamental Research Funds for the Central Universities (22CX07008A). We are also grateful to Changqing Oilfield, PetroChina for providing their in-house database and permission to publish.

occur at the microscale within shales. The lamina-scale diagenetic mass transfer and material redistribution may contribute significantly to effective pore space formation in shales.

INTRODUCTION

As the dominant rock type in the global sedimentary stratigraphic record (Schieber et al., 1998), organic-rich shales have long been regarded as source rocks (Pradier et al., 1991; Löhr et al., 2015). In recent years, the petroleum industry has shifted from conventional to unconventional resource exploration and development with the increasing demand for energy resources (Ross and Bustin, 2008; Jia et al., 2012). As the most important unconventional resource types, shale oil and gas are characterized by source and reservoir in the same formation, namely organic-rich shale simultaneously acting as both source and reservoir (Wilson et al., 2016; Ilgen et al., 2017; Zou et al., 2018; Liu et al., 2019). Diagenesis is the major controlling factor for conventional oil and gas reservoir quality (Morad et al., 2010; Taylor et al., 2010), and is even more important for shale oil and gas reservoirs (Taylor and Macquaker, 2014; Shaldybin et al., 2017; Liu et al., 2022; Zeng et al., 2022). Fluid–rock interaction and diagenetic mass transfer are the most important aspects in reservoir diagenesis research and have been intensively studied in conventional reservoirs (Curtis, 1978; Morad et al., 2000; Bjørlykke and Jahren, 2012; Sample et al., 2017). However, diagenetic alteration in shale oil and gas reservoirs remains limited because of fine-grained particles and complex rock compositions (Milliken and Day-Stirrat, 2013; Macquaker et al., 2014). In particular, the extremely low porosity and permeability of shales make diagenetic alteration and mass transfer studies more difficult than those in sandstone reservoirs (Potter et al., 2005; Yang and Yu, 2022).

The formation of reservoir pores and increase in brittleness are the primary concerns for the efficient exploration and development of shale oil (Loucks et al., 2012; Milliken and Day-Stirrat, 2013; Dong et al., 2017). Pore formation and brittleness variations are determined mainly by authigenic mineral precipitation and detrital grain dissolution (Baruch et al., 2015; Milliken and Olson, 2017; Wu et al., 2019). These processes are related to fluid activity, open or closed system variations, and mass transfer during diagenetic alterations (Schieber et al., 2000; Stixrude and Peacor, 2002; Ghanizadeh et al., 2014; Rimstidt et al., 2017; Liu et al., 2018; Milliken et al., 2018). Among the numerous shale diagenesis studies, authigenic quartz with various silica sources and complex precipitation processes is the most important (Peltonen et al., 2009; Milliken et al., 2016; Dowey and Taylor, 2017; Peng et al., 2020). The dissolution or recrystallization of siliceous organisms has been summarized as the most significant silica source for

authigenic quartz in organic-rich shales, especially marine sedimentary sequences (Schieber et al., 2000; Khalil et al., 2007; Cai et al., 2022). Other silica sources have also been proposed for authigenic quartz growth, such as feldspar dissolution (Milliken and Olson, 2017; Peng et al., 2020), detrital quartz pressure solution (Dowey and Taylor, 2020), and smectite-to-illite transformation (Van de Kamp, 2008; Thyberg and Jahren, 2011; Metwally and Chesnokov, 2012). In lacustrine shales with few siliceous organisms, the nonbiological silica sources may be more important for authigenic quartz precipitation (Zou et al., 2019; Sun et al., 2022). Diagenetic fluid flow and mass transfer are necessary for these reactions to occur in buried shales (Metwally and Chesnokov, 2012; Zhu et al., 2022).

Previous studies have shown that diagenetic fluids and by-products can migrate from shales to interbedded sandstones, resulting in authigenic mineral cementation or detrital grain dissolution in sandstones (Boles and Franks, 1979; Berger et al., 1997; Lynch et al., 1997; Day-Stirrat et al., 2010; Xi et al., 2019). However, it is still debatable whether diagenetic mass transfer can occur in thick shale formations (Metwally and Chesnokov, 2012). Some researchers have regarded shale formation as an open diagenetic system, allowing mass transfer to or from surrounding formations (Awwiller, 1993; Day-Stirrat et al., 2010). Most other researchers, however, claim that the shale formation mainly occurs as closed diagenetic systems, in which mineral precipitation and dissolution reactions must be locally mass balanced (Thyberg et al., 2010; Thyberg and Jahren, 2011; Metwally and Chesnokov, 2012). Although the smectite-to-illite reaction has been proposed as a silica source for authigenic quartz precipitation in shale reservoirs, the mechanisms of diagenetic fluid flow and mass transfer in a closed diagenetic system are not fully understood (Metwally and Chesnokov, 2012; Milliken and Day-Stirrat, 2013; Taylor and Macquaker, 2014). In particular, there is still a lack of direct petrographic or geochemical evidence on how diagenetic fluid flow and mass transfer drive mineral precipitation and dissolution processes in organic-rich shale formations.

In recent years, lacustrine shale oil exploration breakthroughs in China have occurred mainly in laminated shale strata, such as the Cretaceous Qingshankou Formation in the Songliao Basin, the Triassic Yanchang Formation in the Ordos Basin, and the Permian Lucaogou Formation in the Junggar Basin (Sun et al., 2023). Laminated shale has been proven to be the favorable lacustrine shale oil exploration target (Jin et al., 2021). In different lacustrine basins, however, the lamina types and their combination styles are significantly different, resulting in various diagenetic alteration processes and different types of pore spaces (Jiang et al., 2023). The successful prediction on the distribution of effective pores for oil accumulation, based on shale diagenesis and reservoir formation mechanisms, is the main research emphasis in shale oil exploration studies. The objectives of this study were to (1) understand the diagenetic variations in lacustrine organic-rich shales, (2) provide direct evidence of lamina-scale diagenetic mass transfers in organic-rich shales, and (3) provide new insights into the mineral precipitation and dissolution processes in organic-rich shale formations. Based on these studies, the impact of diagenesis on shale oil reservoir formation is discussed further.

GEOLOGIC BACKGROUND

The Ordos Basin is a polycyclic superimposed petroliferous basin located in the western part of the North China platform and has become the largest oil and gas production base in China (Fu et al., 2021). During the Late Triassic Indosinian Orogeny, the compression and collision of the Yangtze and North China plates resulted in the Ordos large depression lacustrine basin (Fu et al., 2021). The basin is bounded to the north by the Yin Mountains, to the south by the Qinling Mountains, to the east by the Lüliang Mountains, and to the west by the Helan-Liupan Mountains (Figure 1B), covering an area of approximately 250×10^3 km^2 (Lai et al., 2016). It can be further subdivided into six tectonic subunits: the Yimeng uplift, the Weibei uplift, the Jinxi flexural fold belt, the western edge thrusting belt, the Tianhuan depression, and the Shanbei slope (Figure 1A).

During the sedimentation of the Yanchang Formation in the Late Triassic, the Ordos Basin changed from a marine and transitional setting to a continental setting (Ji et al., 2010), and a set of fluvial-lacustrine terrigenous clastic sediments were deposited (Zhao et al., 2015). The Yanchang Formation reached more than 1000 m in thickness, recording the entire process of formation, expansion, contraction, and extinction

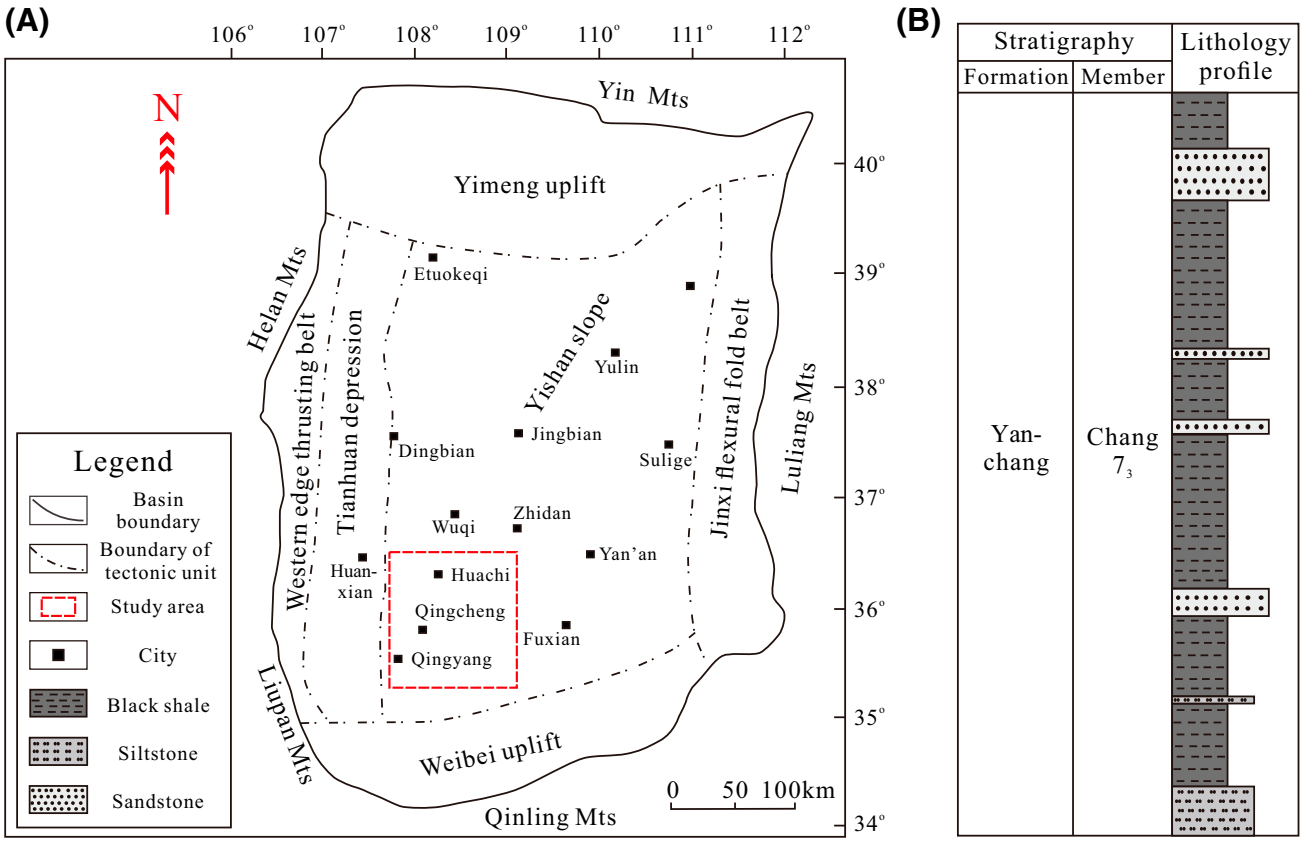

Figure 1. Tectonic subunits of the Ordos Basin and sedimentary stratigraphy of the study interval. (A) Tectonic subunits of the Ordos Basin and the location of study area. (B) Sedimentary stratigraphy of the Yanchang Formation Chang 7_3 submember in the study area. Mts = mountains.

of a large lacustrine system. The formation is divided into 10 members. The Chang 7 member was deposited during the maximum transgression period in the Mesozoic, when the semideep-to-deep lake area was approximately 65×10^3 km^2 (Fu et al., 2021), and algae or plankton bloomed. Thus, large-scale lacustrine organic-rich shales and delta gravity flow sands were deposited (Fu et al., 2020). Furthermore, the Chang 7 member can be divided into three submembers, namely Chang 7_1, Chang 7_2, and Chang 7_3, from top to bottom. Among them, the Chang 7_1 and 7_2 submembers consist mainly of gravity-flow-deposited sandstone bodies (Fu et al., 2020, 2021). During the sedimentary period of the Chang 7_3 submember in the Middle–Late Triassic, the southern part of the Ordos Basin experienced significant subsidence due to the strong collision and rapid uplift of the Qinling orogenic belt. The basin was high in the north and low in the south, with water depth increasing accordingly. In this time, the sedimentary center of the basin was located to the east of Yan'an, Dingbian, Huanxian, and Qingyang. The maximum shoreline during peak transgression extended northwestward to the Etuokeqian Banner area, allowing for the deposition of widespread high-quality, organic-rich lacustrine shale formations that serve as important source rocks, forming a set of organic-rich shale formations (Figure 1B). The Chang 7_3 shale is mainly buried at a depth of approximately 2000 to 3000 m, with a thickness of 28 to 42 m (Xi et al., 2020). The total organic carbon (*TOC*) in the Chang 7_3 submember shales can reach approximately 5.33%–30.69% (Fu et al., 2020), providing favorable conditions for lacustrine shale oil formation, and a billion-ton shale oil field has been proven in this area (Fu et al., 2020).

MATERIALS AND METHODS

This research was based on shale samples from the Cai 30 well area, where most shale oil exploration drilling has taken place (Figure 1A). Shale samples

were prepared for thin sections and microscopic observations. Typical shale samples with authigenic quartz precipitation and feldspar dissolution were then selected for high-resolution scanning electron microscopy (SEM), advanced mineral identification and characterization system (AMICS) analysis, SEM-cathodoluminescence (SEM-CL) analysis, and energy spectrum scanning. Some large-sized authigenic quartz and euhedral pyrite in the above samples were selected to carry out in situ element and stable isotope testing using laser ablation (multicollector)-inductively coupled plasma-mass spectrometry (LA-ICP-MS). Samples with a clear contact interface between the clay mineral agglomerates and organic matter stripes were chosen for nanoscale indentation testing and in situ laser Raman spectrum analysis. In addition, organic geochemical analyses were conducted on different laminae of organic-rich shales using the microdrilling method.

Petrographic Features Analysis

The lamina types and diagenetic alteration characteristics of organic-rich shale were observed using a Zeiss Imaging-2M optical microscope. In situ quantitative analysis of the mineral composition was conducted using an AMICS equipped on a Zeiss Crossbeam 550 focused ion beam (FIB-SEM) with a Bruker energy-dispersive spectrometer (EDS). Freshly prepared thin sections were carbon coated and glued onto aluminum stubs. Then, a quantitative analysis of various mineral phases for each pixel was performed using high-resolution EDS and the AMICS database. Each image scanning was performed using 20-nm resolution under the EDS probe for approximately 12 hr. From the AMICS analysis, two-dimensional images showing the reservoir rock mineral compositions and their spatial distribution were obtained.

The micromorphology of the clay minerals, authigenic quartz, euhedral pyrite, and feldspar dissolution features were observed using a Zeiss Crossbeam 550 FIB-SEM. The samples were polished for approximately 8 hr by Ar-ion-beam milling using a Gatan 685.C. Typical SEM images were captured with a working distance (WD) of 12 mm, an accelerating voltage of 15 V, and a current of 1.0 nA. Authigenic quartz was detected using a Gatan Monarc CL detector equipped with a Zeiss Crossbeam 550 FIB-SEM. The luminescence wavelength ranged from 250 to 800 nm. Digital monochromatic CL images were captured with a beam current of 2.0 nA, an accelerating voltage of 5.0 kV, and an average WD of 22 mm. Based on the gray value differences of the monochromatic CL images, the CL spectrum was captured at different sites of authigenic quartz, with a dwell time of 20 s and a step size of 10 nm.

The degrees of smectite-to-illite transformation and authigenic quartz crystallization were evaluated by LabRAM HR Evolution high-resolution laser Raman spectroscopy equipped with an Olympus microscope. A standard Si sample was used to calibrate the instrument by matching the 520.1 cm^{-1} wavelength position. Laser Raman spectrum testing was conducted at an excitation wavelength of 325 nm, and the laser spot size was approximately 2.0 μm. To fully access key information on clay minerals and authigenic quartz, the wavelength of the spectrum was limited to the range of 200 to 1000 cm^{-1}.

Micromechanical Property between Different Laminae

The in situ elastic modulus and hardness on the microscale were analyzed using a Bruker TI Premier NanoIndentor with a pressure of 1 to 10,000 μN and an indentation depth of 0 to 3 μm. The polished samples prepared as double-thick thin sections of approximately 70 to 80 μm were used for nanoindentation testing. All of the tests were programmed in load control mode so that the indenter could contact the sample surface at a maximum load of 3500 μN. The spacing between each indentation was set to 20 μm to obtain the microanisotropy of the elastic modulus and hardness of the shales accurately. Then, the in situ elastic modulus and hardness were tested through a double-thick thin section using the 20-μm spacing as step interval. The first type of test points were chosen on the interface of clay agglomerate and organic matter stripe, whereas the others distributed inside of the clay agglomerate. Finally, the in situ elastic modulus and hardness of two types of test points could be compared to each other.

Element and Isotope Geochemistry Analysis

The trace element content in authigenic quartz and shale laminae was determined using LA-ICP-MS.

The analytical conditions and operating procedures for LA-ICP-MS were described by Liu et al. (2008). Laser sampling was performed using GeoLas 2005, and the ion signal intensities were measured using an Agilent 7500a ICP-MS instrument. The elemental contents were calibrated using multiple reference materials (National Institute of Standards and Technology [NIST] SRM 610, NIST SRM 612, BCR-2G, BIR-1G, and BHVO-2G). The test site was carefully selected on authigenic quartz crystals and different laminae to ensure accurate measurement of elements of geochemical interest. The spot size in the single-point ablation mode was 20 μm. Signal selection and time drift correction were performed using ICPMS-DataCal (Liu et al., 2008, 2010). In addition, energy spectrum scanning under a Zeiss Crossbeam 550 FIB-SEM equipped with a Bruker EDS was used to characterize the element distribution heterogeneity in the different shale laminae. The shale samples with apparent contact interfaces between different laminae were selected to analysis K and Si content on the line scan model. The scanning step in the direction perpendicular to the laminae is 1.0 μm.

In situ S isotope analysis of pyrites was used to determine the different origins of framboid pyrite and scattered euhedral pyrite. This analysis was performed using a Nu Plasma 1700 LA-ICP-MS with a 193-nm excimer laser denudation system (RESOlution m-50, ASI). Detailed analytical procedures were performed as described by Chen et al. (2017) and Bao et al. (2017). The single-point ablation mode was adopted and the key analyzed parameters were set as a laser energy fluence of 3.6 J/cm^2, frequency of 3 Hz, and spot size of 25 μm. The carrier gas was 280 mL/min high-purity helium, and the supplement gas was 0.86 L/min Ar. The S isotopic composition is expressed as a relative value:

$$\delta^{34}S = [(^{34}S/^{32}S_{sample})/(^{34}S/^{32}S_{standard}) - 1] \times 1000 \quad (1)$$

IAEA-S-1, which is Ag_2S with $\delta^{34}S_{V\text{-}CDT}$, known to be −0.3‰, was used as the standard sample.

Organic Geochemistry Analyses

Organic geochemical analyses were performed on whole-rock samples of the Chang 7_3 submember and microdrilling samples from different laminae of the organic-rich shales. To obtain microdrilled samples, first, the bulk shale samples were polished to distinguish different types of laminae. Second, a 100-μm drill equipped on a stereoscopic microscope was used to collect powder samples from different shale laminae. Powder samples were used for bulk geochemical parameter pyrolysis, bitumen extraction, molecular analysis, and organic acid compound analysis. For whole-rock samples, oil was extracted with dichloromethane/methanol (93:7, v:v) using an accelerated solvent extractor (ASE, Dionex ASE-200). For the microdrilled samples, bitumen was extracted using ultrasonic treatment. Briefly, microdrilled powders were dissolved in 30 mL of solvent, ultrasonicated for 20 min, and left to stand for 12 hr. The entire process was repeated, and the solutions were collected. The organic acidic compounds in the bitumen were analyzed using Bruker 9.4T solariX XR Fourier transform-ion cyclotron resonance MS (FT-ICR MS). Electrospray ionization (ESI) coupled with FT-ICR MS allows for the ultrahigh mass resolution identification of acidic heteroatomic compounds. For semiquantitative characterization, tetradecanoic-D27 acid was added as an internal acidic standard. The oil was then subjected to group fractionation to separate saturates, aromatics, resins, and asphaltenes. The molecular composition of bitumen was analyzed by gas chromatography–mass spectrometry (GC-MS; Agilent 8890 gas chromatograph coupled with a 5977 B mass spectrometer) of the saturated and aromatic fractions. Bulk geochemical parameters were analyzed using a Rock-Eval 7 instrument (VINCI Technologies) on both the unextracted and extracted samples.

Among the above experiments, petrographic analyses, including thin section, SEM, EDS, AMICS, SEM-CL, nanoindentation, high-resolution laser Raman spectroscopy, and energy spectrum scanning, were performed at the Key Laboratory of Deep Oil and Gas, China University of Petroleum (East China). Trace element analysis by LA-ICP-MS was conducted at the Institute of Geochemistry, Chinese Academy of Sciences (CAS; Guiyang). In situ S isotope analysis was performed at the State Key Laboratory of Continental Dynamics, Northwest University. For the organic geochemistry analysis, GC-MS was performed at the Key Laboratory of Deep Oil and Gas, China University of Petroleum (East China). Rock-Eval analysis, hydrocarbon extraction, and acidic compound testing were

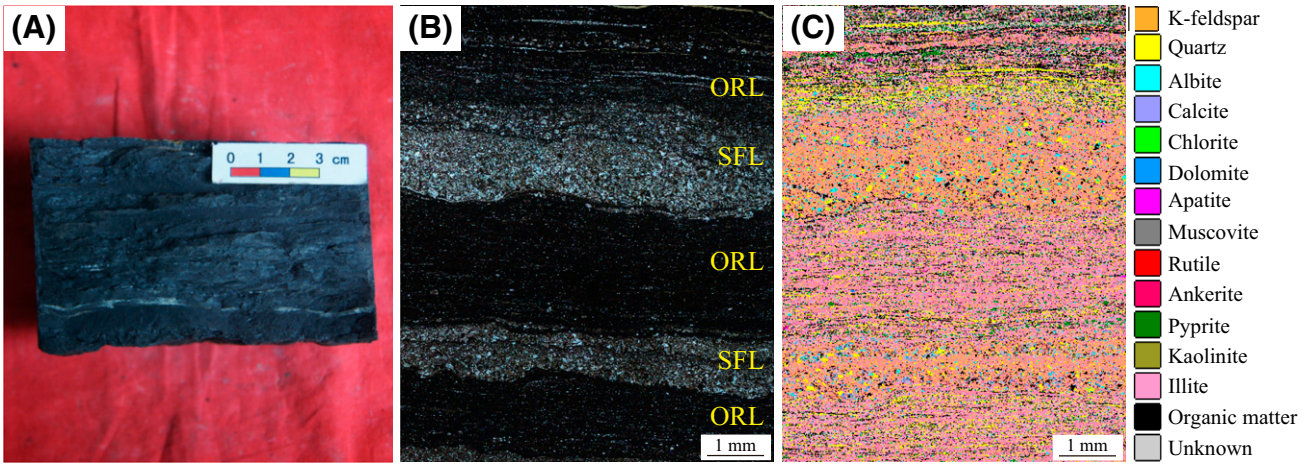

Figure 2. Petrographic characteristics of the organic-rich shale in the Yanchang Formation Chang 7_3 submember. (A) The core sample showing the black color and horizontal bedding, Cai 30, 1964.88 m (6446.46 ft). (B) The thin section micrographic image showing lamina combination of organic-rich lamina (ORL) and silt-sized felsic lamina (SFL) in the organic-rich shales, Cai 30, 1964.88 m (6446.46 ft). (C) The in situ quantitative analysis on mineral composition idem with (B), Cai 30, 1964.88 m (6446.46 ft).

performed at the Guangzhou Institute of Geochemistry, CAS.

RESULTS

Petrographic Characteristics of Laminated Shales

The Yanchang Formation Chang 7_3 submember organic-rich shales are characterized by their black color and horizontal bedding in the core samples (Figure 2A). However, these black shales are quite heterogeneous under a microscope, consisting of two different laminae at the micron-to-millimeter scale (Figure 2B). The mineral composition, organic matter content, and grain size distribution are significantly different between the two types of laminae (Figure 2C; Table 1). The light-colored laminae are dominated by K-feldspar, with a content of up to 68.6% (Figure 2C; Table 1). Quartz and albite are the other important minerals, with contents of approximately 8.8% and 6.2%, respectively (Figure 2C; Table 1). The total clay mineral content is relatively low, mainly including 7.0% kaolinite and 4.1% illite (Figure 2C; Table 1). Several types of minor minerals, less than 1.0%, are also identified in the light-colored laminae—that is, chlorite, pyrite, muscovite, apatite, and rutile (Figure 2C; Table 1). Some scattered organic matter exists in this laminae, but its content is only approximately 3.5% (Figure 2C; Table 1). The detrital grains in the light-colored laminae are mainly silt size (Figure 2A, B); therefore, it is called silt-sized felsic laminae (SFL). The dark-colored laminae mainly consist of illite, clay-sized quartz, clay-sized K-feldspar, and pyrite, with contents of approximately 55.1%, 12.0%, 7.2%, and 9.6%, respectively (Figure 2C; Table 1). Other minor minerals include albite, chlorite, muscovite, apatite, and rutile (Figure 2C; Table 1). The total organic matter content of the dark-colored laminae is approximately 14.0% (Figure 2C; Table 1). Thus, it is defined as an organic-rich laminae (ORL).

Table 1. The Mineral Composition of the Silt-Grained Felsic Lamina and Organic-Rich Lamina

Mineral	Content in Silt-Grained Felsic Lamina, %	Content in Organic-Rich Lamina, %
K-feldspar	68.56	7.22
Quartz	8.79	11.99
Albite	6.15	1.40
Dolomite	0.21	0.14
Chlorite	0.03	0.06
Kaolinite	7.03	0.03
Illite	4.13	55.06
Pyrite	0.94	9.58
Muscovite	0.25	0.24
Apatite	0.35	0.23
Rutile	0.03	0.06
Organic matter	3.53	13.99

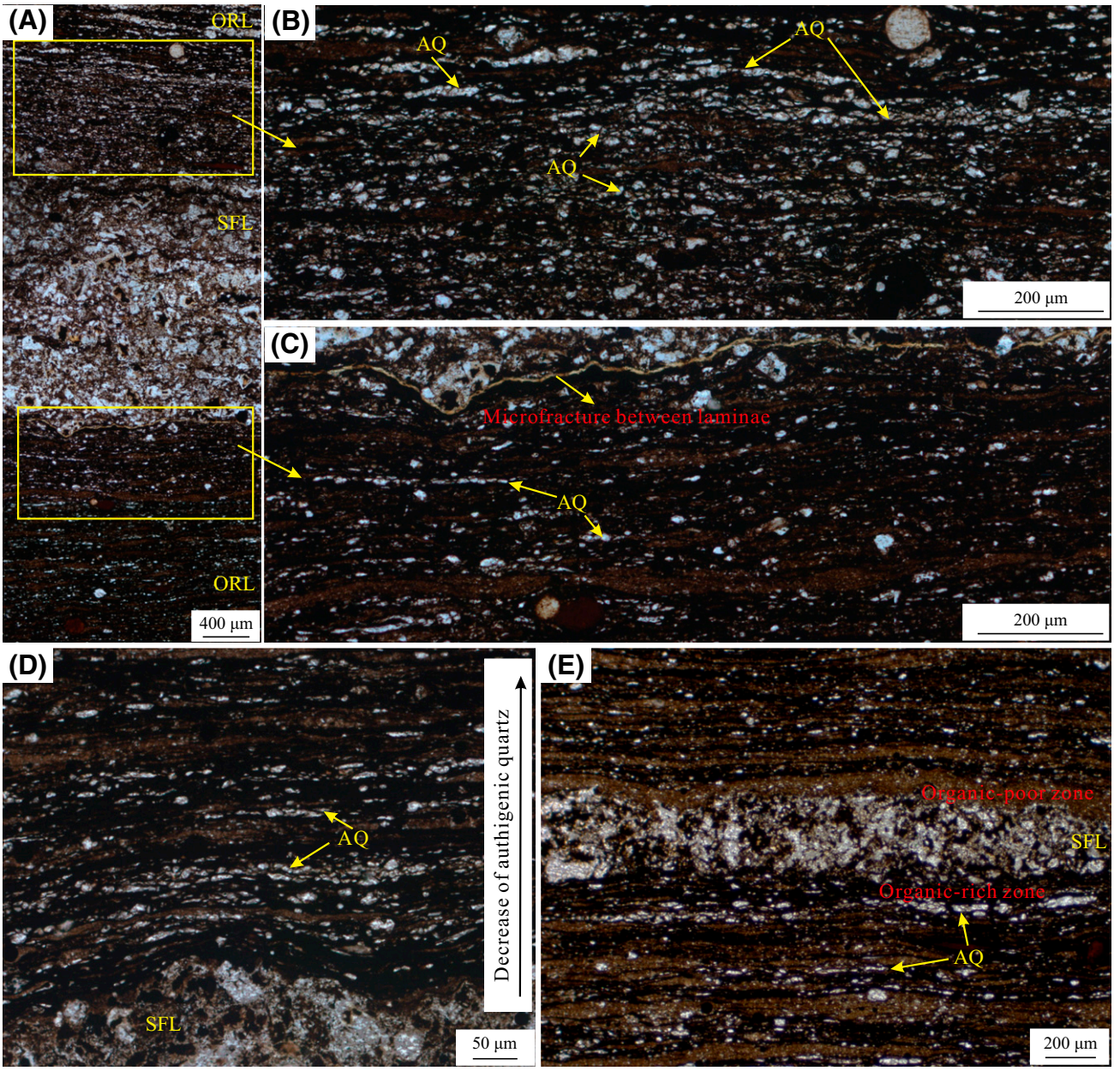

Figure 3. Micro-occurrence and distribution characteristics of authigenic quartz in the Yanchang Formation organic-rich shales. (A) Micrographic image showing distribution of authigenic quartz (AQ) in the organic-rich lamina (ORL). (B) AQ distribution in the ORL without microfracture between it and silt-sized felsic lamina (SFL), Cai 30, 1964.88 m (6446.46 ft). (C) AQ distribution in the ORL with a microfracture between it and SFL, Cai 30, 1964.88 m (6446.46 ft). (D) Micrographic image showing the content of AQ decrease with increasing distance to adjoining SFL, Cai 30, 1964.88 m (6446.46 ft). (E) Micrographic image showing the differences of AQ growth in organic-rich and organic-poor areas, Cai 30, 1964.88 m (6446.46 ft).

Diagenetic Mineralogy in ORL

Authigenic Quartz

Authigenic quartz is the major diagenetic mineral in organic-rich shales and generally develops in the ORL (Figures 2C, 3A). The distribution of authigenic quartz is closely related to the SFL and organic matter. In the ORL, authigenic quartz is distributed as a continuous or quasicontinuous banded occurrence and is centered adjoining the SFL (Figure 3A, B). When a microfracture occurs between the ORL and SFL (Figure 3C), the content of authigenic quartz in the ORL is observably lower than that on the other side without a microfracture (Figure 3A–C). In a single ORL, the

authigenic quartz content decreases with increasing distance from the adjacent SFL (Figure 3D). In addition, the distribution of organic matter has had significant impacts on the development of authigenic quartz in the shale laminae. If the SFL is in contact with the organic-poor clay agglomerates, then authigenic quartz precipitation is rarely observed (Figure 3E). However, on the other side of the organic-rich zone, authigenic quartz growth is clearly associated with organic matter (Figure 3E).

High-resolution SEM analysis indicates that each authigenic quartz band in the ORL consists of several lenticular microcrystals (Figure 4A). Furthermore, these microcrystals are not in close contact with one another but preserve many micropores (Figure 4B). This means that open microfractures always exist between illite agglomerates and organic matter stripes in the ORL, and authigenic quartz is correctly distributed along the microfractures between illite and organic matter (Figure 4C, D). Some microfractures between illite and organic matter are completely filled with authigenic quartz (Figure 4C), whereas others are not fully occupied (Figure 4D). The quartz shows more idiomorphic shapes in the partly filled microfractures than in the completely filled microfractures (Figure 4C, D).

In situ elemental analyses indicate that several common elements, trace elements, and rare earth elements (REEs) are mixed into authigenic quartz. The relative content of Al_2O_3 is higher than those of

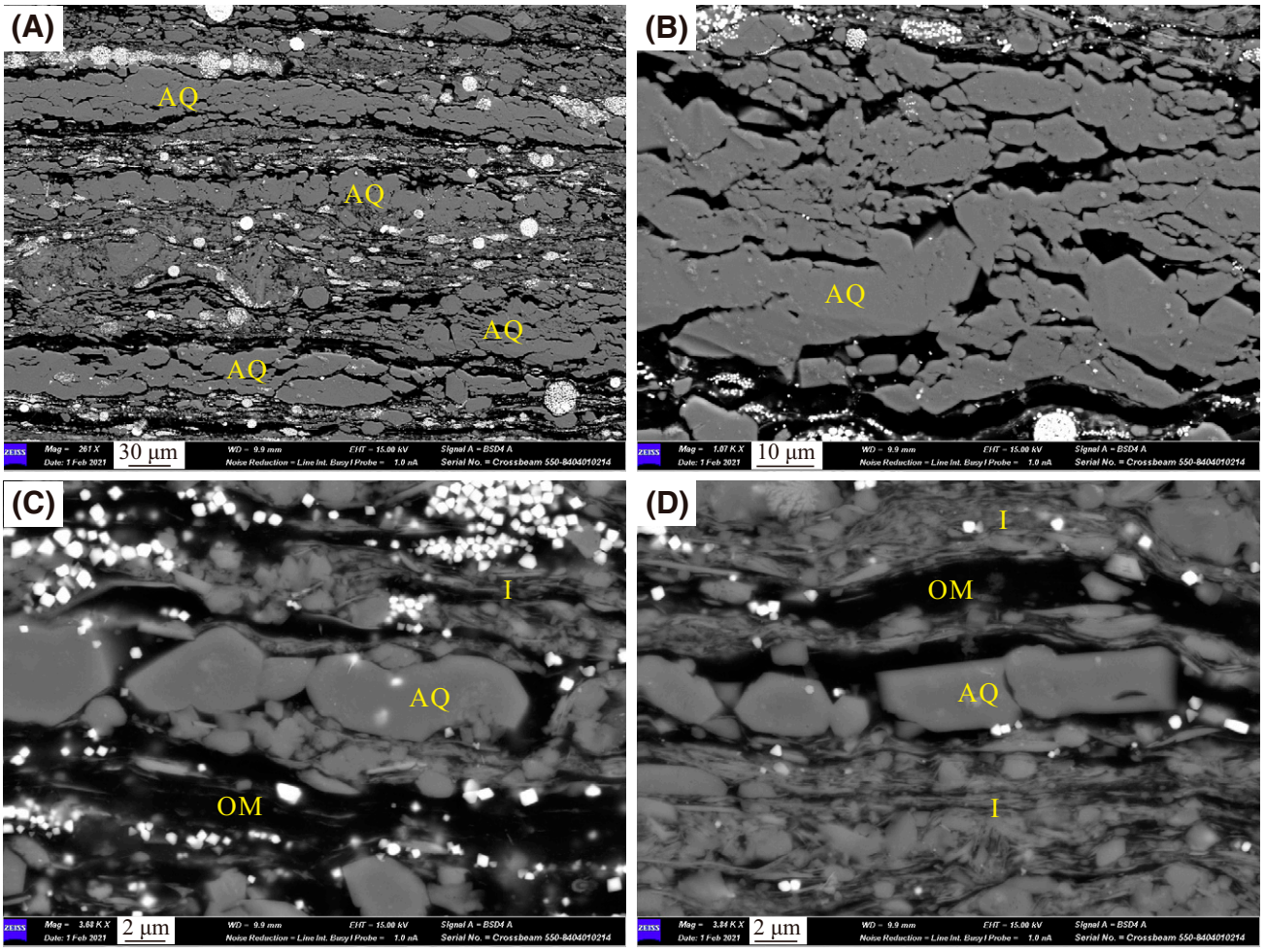

Figure 4. Micrographic images of scanning electron microscopy showing authigenic distribution characteristics in the Yanchang Formation organic-rich shales. (A) The authigenic quartz (AQ) band consists of several lenticular microcrystals in the organic-rich lamina (ORL), Cai 30, 1964.88 m (6446.46 ft). (B) The microcrystals of AQ are not in close contact with one another, preserving micropores, Cai 30, 1964.88 m (6446.46 ft). (C, D) The AQ partly or completely fill in the microfractures, Cai 30, 1964.88 m (6446.46 ft). I = illite; OM = organic matter.

K_2O and Na_2O, and Fe has a higher concentration than Ca and P. Trace elements in authigenic quartz are lower than those in the North American shale composite (NASC), with a ratio of less than 1.0 (Figure 5A). Among the NASC-normalized trace elements, As, Sr, and U have slightly positive anomaly characteristics, but Cr, Zr, and Hf seem to have negative anomalies in some samples (Figure 5A). The NASC-normalized REE patterns are shown in Figure 5B. The REE in authigenic quartz is at lower overall concentrations than in NASC and nearly has patterns parallel to NASC with no distinct redistribution (Figure 5B).

Euhedral Pyrite

Two types of pyrite, framboidal pyrite and scattered euhedral pyrite, have developed in the organic-rich shales of the Yanchang Formation. In general, framboidal pyrite is used to reflect the sedimentary environment (Rickard, 2019), whereas scattered euhedral pyrites are regarded mainly as diagenetic products during burial processes (Jautzy et al., 2020). In the ORL, the distribution of scattered euhedral pyrite is always related to organic matter and authigenic quartz (Figure 6A). The scattered euhedral pyrite has always developed around authigenic quartz or has been embedded in organic matter (Figure 6A, B). Some pyrite particles have even replaced the authigenic quartz (Figure 6A, B). Euhedral pyrite occurs mainly as octahedrons (Figure 6C) and sometimes as pyritohedrons (Figure 6D). Moreover, some lamellar illite has been accompanied by pyritohedral pyrite (Figure 6D). In situ S isotope analyses show that the $\delta^{34}S$ values are significantly different between framboidal pyrite and scattered euhedral pyrite. In two typical samples, the $\delta^{34}S$ values of framboidal pyrite are −2.33‰ and 1.06‰ (Figure 6E, F), whereas they are 5.68‰ and 6.46‰ in scattered euhedral pyrite (Figure 6E, F).

Clay Mineral Alterations

Illite is the dominant clay mineral in the Yanchang Formation organic-rich shale (Figure 2C; Table 1). A small amount of ordered mixed-layer illite-smectite, kaolinite, and chlorite is also noted. Illite has developed in lamelliform or foliaceous shapes, and some microquartz has filled the intercrystal pores (Figure 7A). Based on the petrographic analysis, three samples with the same laminae types and combination styles at different burial depth were selected from wells C30, L57, and G292 (Figure 7B). The studied samples have the same provenance and have similar rock composition, dominated by smectite and illite in clay minerals (Lin et al., 2023). According to the x-ray diffraction (XRD) analysis, the distance between peaks I and II in the diffraction spectrum decreases with increasing burial depth of the samples (Figure 7B), indicating an increased degree of transformation of smectite to illite (Inoue et al., 1987, 1992). From 1600 to 2400 m, the content of mixed-layer illite-smectite decreases with increasing burial depth (Figure 8A). In contrast, the illite content shows an increasing trend with burial depth (Figure 8B). However, chlorite content does not vary significantly with increasing burial depth (Figure 8C). Mixed-layer illite-smectite interstratified with $R = 3$ (where R represents the degree of order in smectite to illite

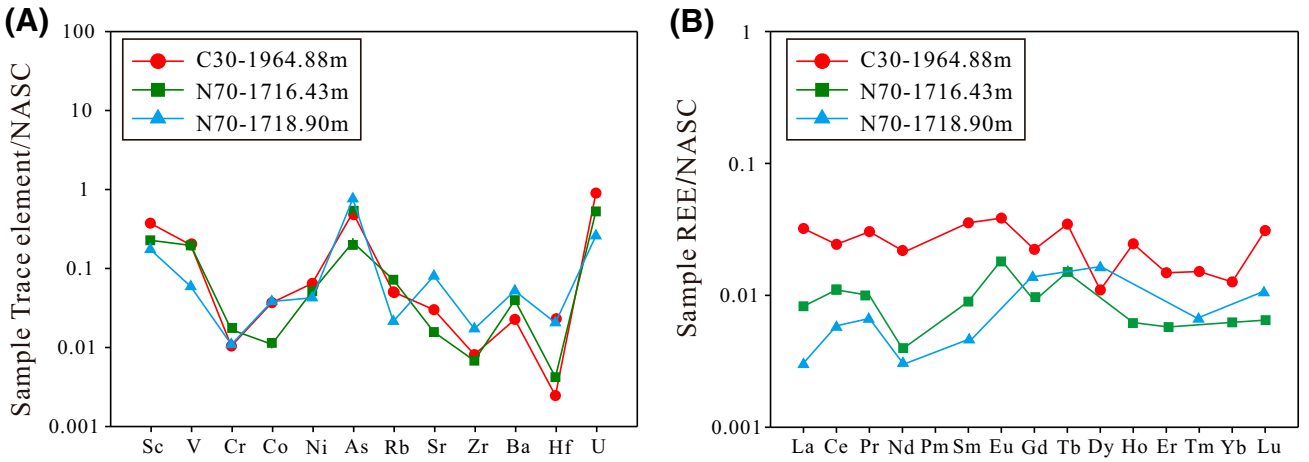

Figure 5. Element geochemistry of the authigenic quartz. (A) The spider diagram of trace elements in authigenic quartz. (B) The North American shale composites (NASC) normalized rare earth element (REE) patterns in authigenic quartz.

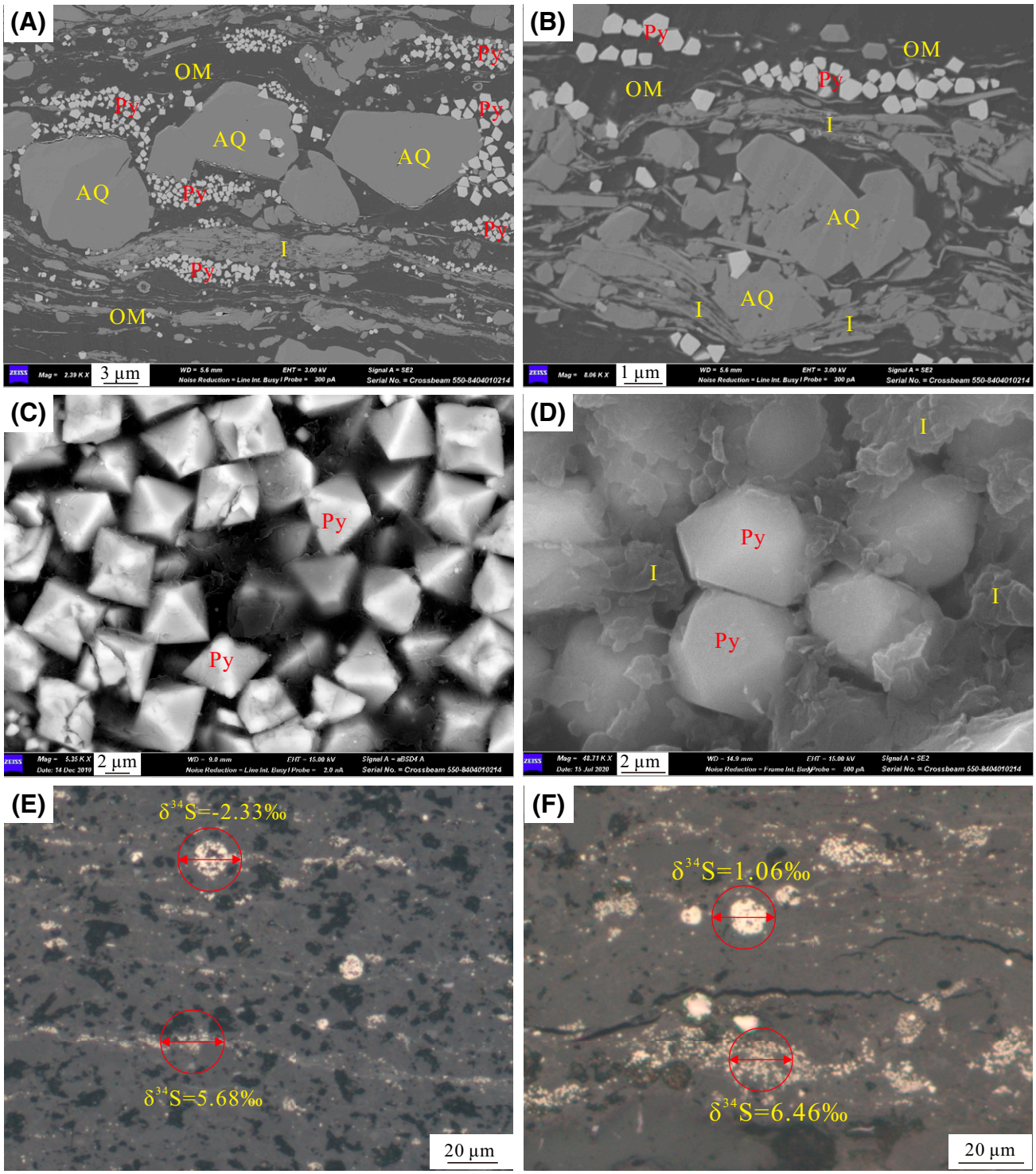

Figure 6. Petrographic and sulfur isotopic characteristics of pyrite (Py) in the Yanchang Formation organic-rich shales. (A, B) Micrographic images of scanning electron microscopy (SEM) showed that scattered Py distributed together with organic matter (OM) and authigenic quartz (AQ), Cai 30, 1964.88 m (6446.46 ft). (C) Micrographic images of SEM showing octahedron Py, Cai 30, 1959.48 m (6428.74 ft). (D) Micrographic images of SEM showing pyritohedron Py and the related lamellar illite (I), Ning 70, 1719.07 m (5639.99 ft). (E) The in situ S isotope testing on framboidal Py and scattered euhedral Py, Cai 30, 1966.5 m (6451.77 ft). (F) The in situ S isotope testing on framboidal Py and scattered euhedral Py, Ning 70, 1714.96 m (5626.51 ft).

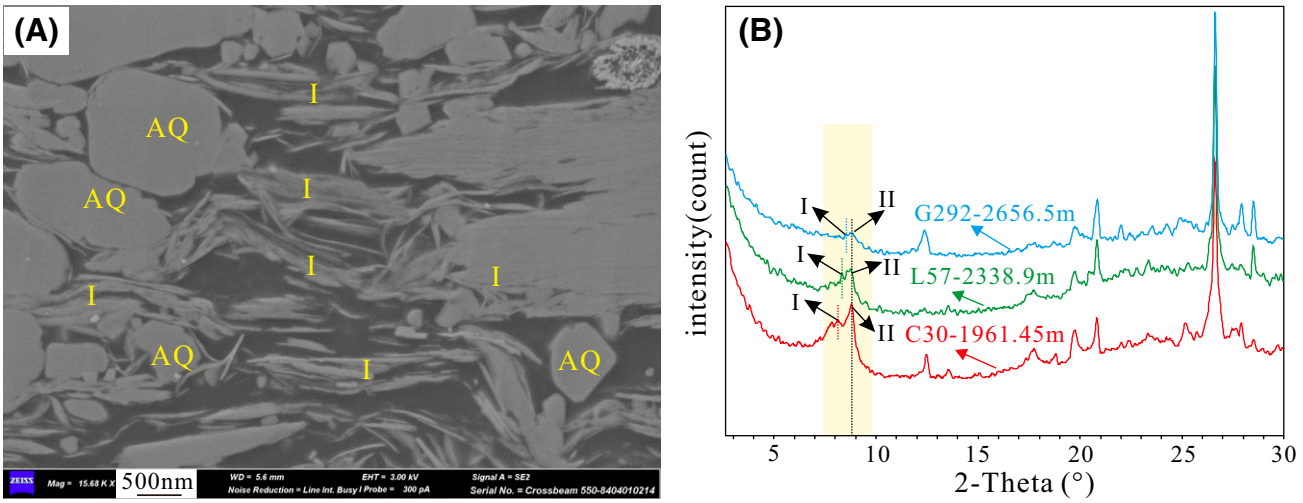

Figure 7. Petrographic observation and x-ray diffraction (XRD) analysis of illite (I) in the organic-rich shales. (A) Micrographic image of scanning electron microscopy showing the foliaceous illite and the associated microquartz crystals, Cai 30, 1964.88 m (6446.46 ft). (B) The clay fraction XRD spectrum of the shale samples from Cai 30, 1961.45 m (6435.20 ft), Li 57 2338.9 m (7673.56 ft), and G 292, 2656.5 m (8715.55 ft) at different burial depth showing that the transformation degree of smectite to illite increased with increasing burial depth. AQ = authigenic quartz.

transformation reaction) developed throughout the study intervals, characterized by an illite percentage (I%) higher than 85% (Figure 8D). Below approximately 2000 m, the I% in the mixed-layer illite-smectite is up to 95% (Figure 8D), indicating that most of the smectite was transformed to illite.

K-Feldspar Dissolution in SFL

The K-feldspar grains commonly experienced partial or complete dissolution in the SFL of organic-rich shales (Figure 9A–C). The dissolution occurs mainly in the interior of the K-feldspar grains, forming

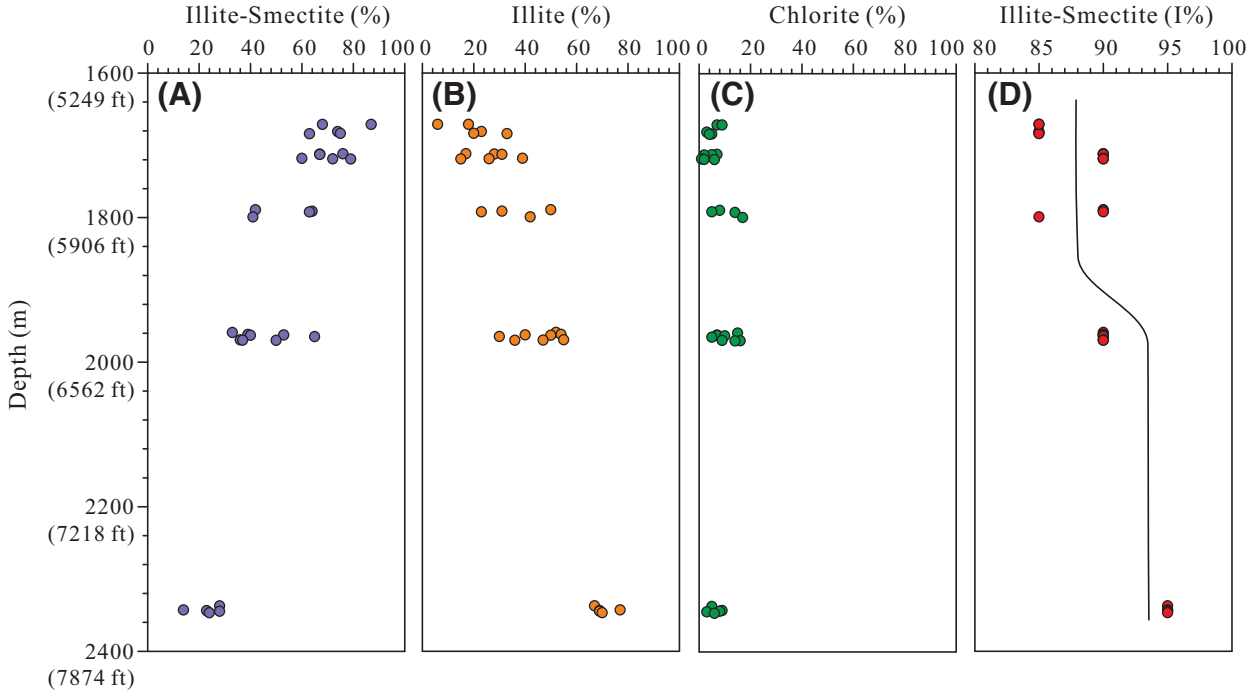

Figure 8. The content variation of clay minerals with respect to burial depth of the Yanchang Formation organic-rich shales. (A) The content of illite/smectite varies with burial depth. (B) The content of illite varies with burial depth. (C) The content of chlorite varies with burial depth. (D) The percentage of illite in mixed layer illite-smectite varies with burial depth. The results showed that ordered mixed-layer illite-smectite and illite increased with increasing burial depth, whereas random mixed-layer illite-smectite decreased with increasing burial depth.

intragranular pores (Figure 9A, B). Petrographic evidence shows that most of the K-feldspar grains in the SFL have dissolved to form secondary pores (Figure 9A, B). Meanwhile, booklet-shaped kaolinite is observed in the K-feldspar dissolution pores, and the intercrystal pores are largely preserved (Figure 9D). The size of the dissolution pores ranges from dozens to hundreds of micrometers (Figure 9A–C), almost always charged by crude oil (Figure 9A, B, D).

Organic Geochemistry Characteristics of Laminated Shales

Oil and Acidic O Compounds in Different Laminae

Organic geochemistry testing experiments were conducted on microdrilling samples from the SFL and ORL of the studied shales. The rock sample from position I refers to the SFL, whereas position II and position III represent the ORL (Figure 10A–C). The ESI FT-ICR MS analysis shows that several kinds of acid compounds are detected in the extracted organic matter (*EOM*), mainly including O_2–O_5 compounds. It has been concluded that O_2–O_5 compounds contain at least one carboxyl (–COOH) in their chemical structure, supporting the idea that organic acids are generated during the thermal evolution of organic matter (Tomczyk et al., 2001). Compared to the ORL samples, SFL contains more O_2–O_5 compounds (Table 2). In the microdrilling sample from position I, the total O_2–O_5 can reach up to 158.26 μg/g (Table 2), whereas they decrease to 77.69 and 32.97 μg/g in positions II and III, respectively (Table 2).

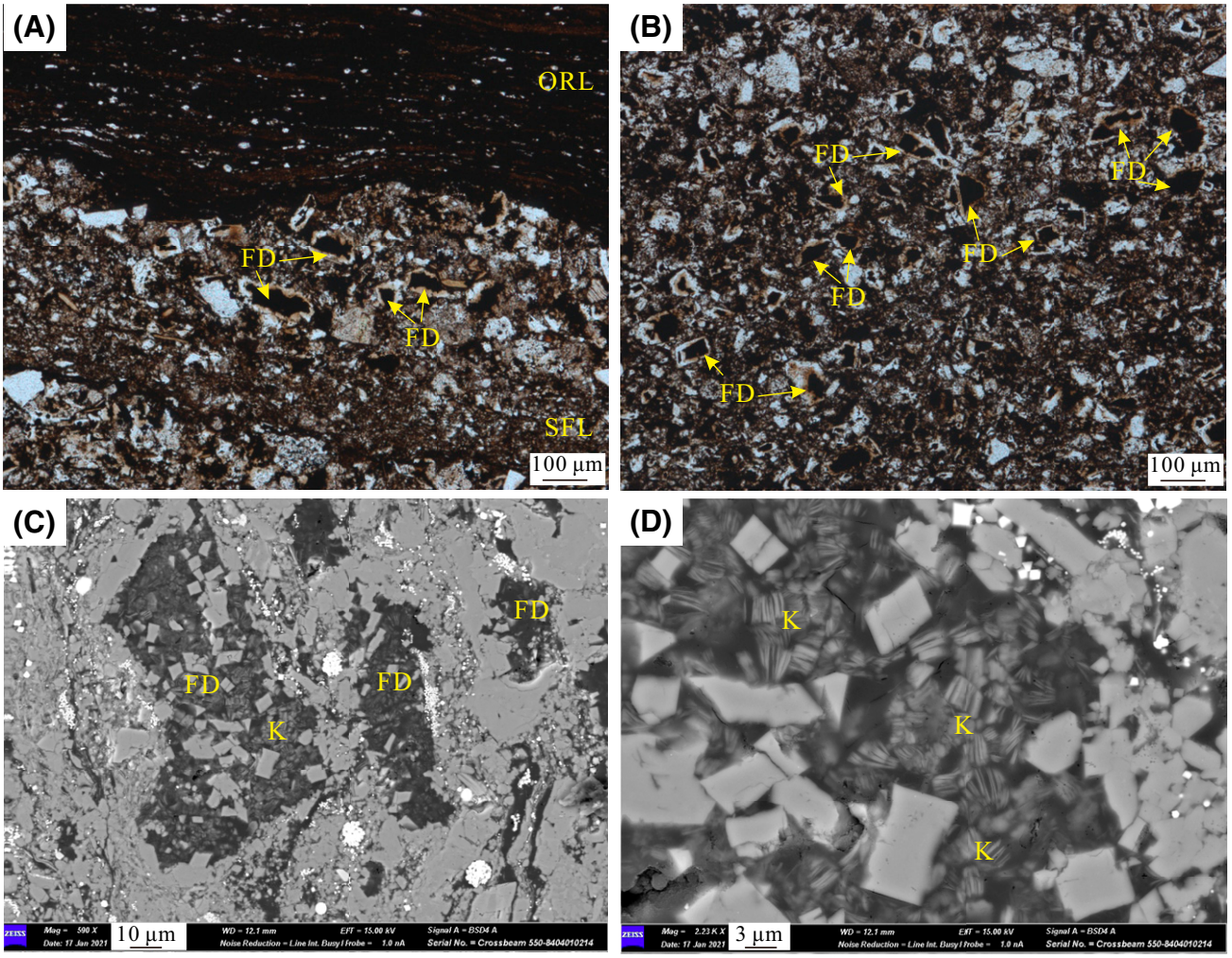

Figure 9. Feldspar dissolution characteristics in the silt-sized felsic lamina (SFL) of the Yanchang Formation organic-rich shales. (A, B) Micrographic images of thin section showing extensive K-feldspar dissolution (FD), Cai 30, 1964.88 m (6446.46 ft). (C, D) Micrographic images of scanning electron microscopy showing FD and kaolinite (K) precipitation, Cai 30, 1959.48 m (6428.74 ft). ORL = organic-rich lamina.

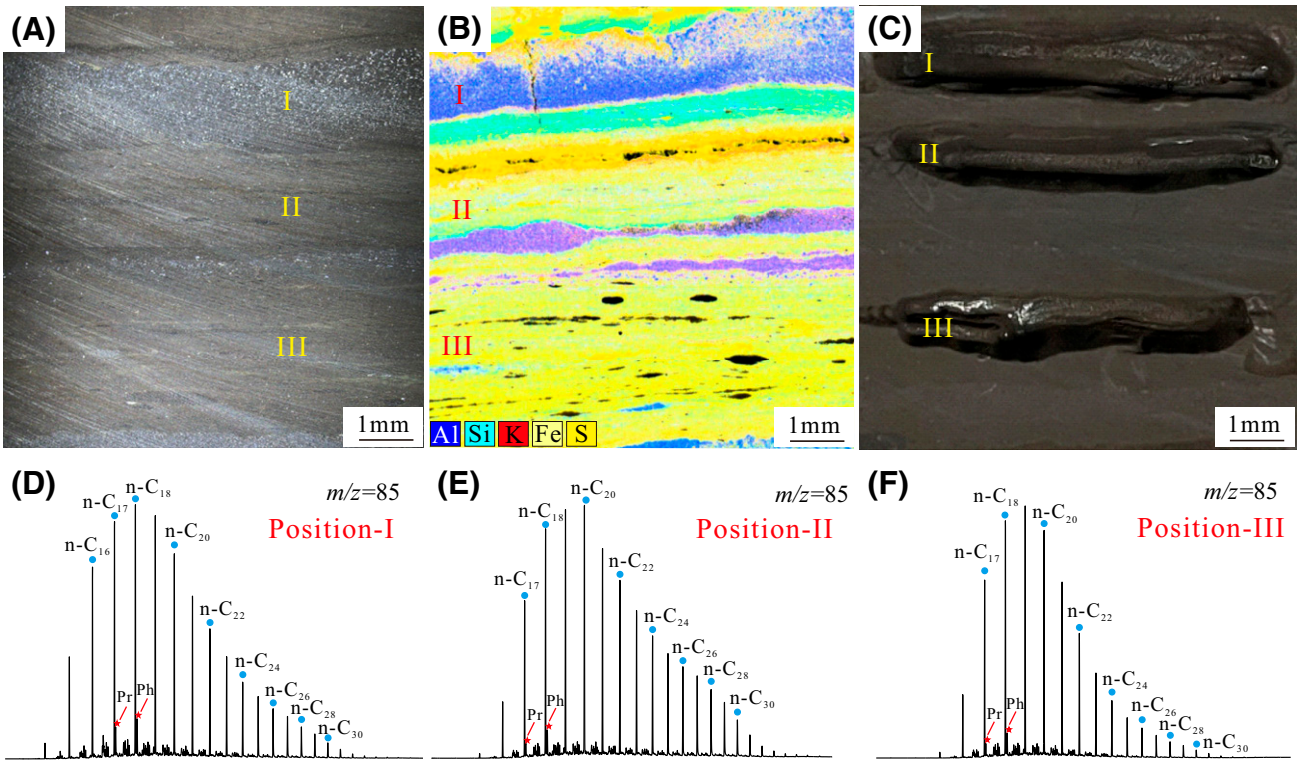

Figure 10. Organic geochemistry analysis of the Yanchang Formation organic-rich shales. (A–C) Microdrilling samples collection in the silt-sized felsic lamina (SFL) and the organic-rich lamina (ORL), Ning 70, 1720.95 m (5646.16 ft). (D–F) The n-alkanes distribution characteristics in the samples from SFL and ORL, showing that the n-alkanes distribution was similar in the SFL and ORL. *m/z* = mass-to-charge ratio; Ph = phytane; Pr = pristane.

According to hydrocarbon extraction and Rock-Eval analysis, *TOC* in position I is obviously lower than that in positions II and III (Table 3). Nevertheless, the values of *EOM*, S_1/TOC (where S_1 represents free hydrocarbons), *EOM/TOC*, and saturated hydrocarbons are higher in position I than in positions II and III (Table 3). This means that the free hydrocarbon content is higher in the SFL than in the ORL, although it has a lower *TOC* value in the SFL. The n-alkanes show unimodal distribution characteristics in the samples from both the SFL and ORL (Figure 10D–F). In the SFL, the lower carbon number n-alkanes are more enriched and mainly centered on C_{16}–C_{18} (Figure 10D). By comparison, the carbon numbers of n-alkanes in the ORL are slightly right moving, with a carbon number peak centered on C_{18}–C_{20} (Figure 10E, F). The $\sum C_{21-}/\sum C_{22+}$ value in position I is 1.10, which is obviously lower than 2.26 in position II, indicating that the light n-alkanes are more concentrated in the SFL than the adjoining ORL. Compared to ORL, the *TOC* of SFL is lower. However, the oil content indicators of *EOM*, S_1/TOC, and *EOM/TOC* are higher in SFL. Therefore, it is presumed that the SFL has received oil charge from the ORL. During the expulsion and migration process, light normal alkanes were preferentially expelled and migrated from the ORL and then accumulated in the SFL.

Table 2. The Results of the Acid Compounds Analysis in the Silt-Sized Felsic Lamina and Organic-Rich Lamina

	Content of Acid Compounds in Rocks, μg/g		
Compounds	I	II	III
O_2	35.30	16.96	10.30
O_3	34.03	17.52	7.19
O_4	62.78	29.51	10.59
O_5	26.16	13.70	4.89
Total O_2–O_5	158.26	77.69	32.97

GC-MS Molecular Parameters in Shale System

A total of 12 core samples consisting of shale and sandstone were collected within one well, with depth intervals ranging from 1957 to 1971 m (Figure 11). The upper thick shale interval mainly consists of an ORL with a minor SFL. Downward, the occurrence of SFL gradually increases and the thickness also increases.

Table 3. The Results of Hydrocarbon Extraction and Rock-Eval Analysis in the Silt-Sized Felsic Lamina and Organic-Rich Lamina

Position	*TOC*, %	*EOM*, mg/g Rock	S_1/*TOC*, mg/g	*EOM*/*TOC*, mg/g	Saturated Hydrocarbon
I	10.12	8.14	40.22	80.43	25.52
II	19.08	5.07	23.38	26.59	18.45
III	28.02	5.98	23.34	21.35	13.23

Abbreviations: *EOM* = extracted organic matter; *TOC* = total organic carbon.

Furthermore, the sediments become thin layers of interbedded silt-to-sandstone and shale, and finally, thick silt-to-sandstone with tear-shaped mudstone debris. Interestingly, the three saturated component-derived molecular parameters $\sum C_{21-}/\sum C_{22+}$, relative pregnane content, and Ts/hopane (where Ts represents C27-18α-22,29,30-trisnorneohopane) in the lower shale interval (laminated shale enriched with SFL) are generally greater than those in the upper shale interval (shale lacking SFL).

DISCUSSION

Biogenic Silica Nucleation for Authigenic Quartz Growth

Previous studies have commonly claimed that authigenic quartz growth requires silica nucleation sites; for example, detrital quartz grains with clean surfaces

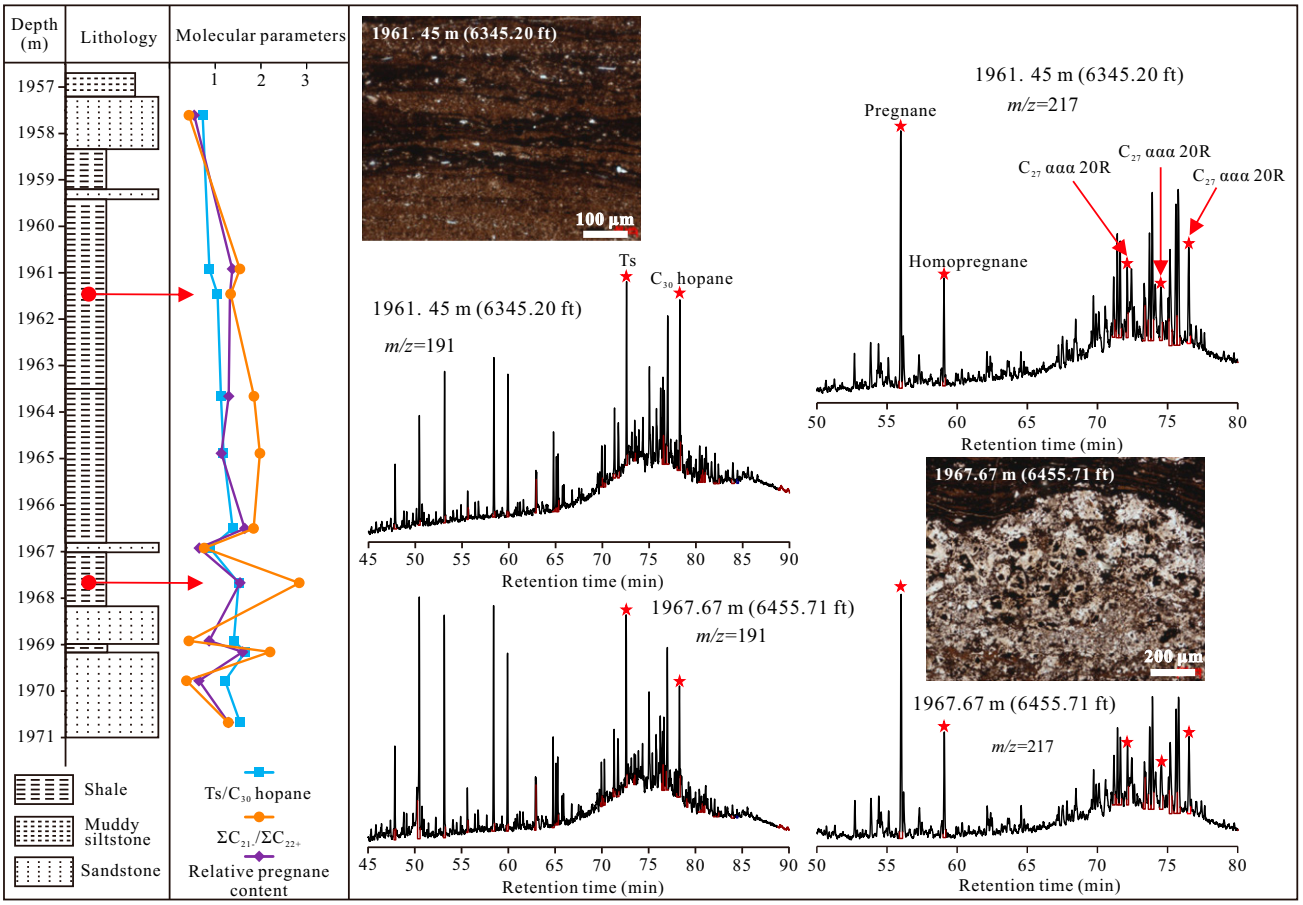

Figure 11. Profile of chain-breaking reaction-related molecular ratios with depth and the gas chromatography–mass spectrometry chromatograms showing specific saturated compounds used to calculate the ratios in the well Ning 70. To make the trend more obvious, Ts/C30 hopane was multiplied by 2. Ts and C30 hopane are hopane compounds measured using mass-to-charge ratio (*m/z*) 191 chromatogram. Ts is short for C27-18α-22,29,30-trisnorneohopane, C30 hopane stands for C29-17α (H),21β(H)-hopane. Pregnane, homopregnane, C27 ααα 20R, C28 ααα 20R, and C29 ααα 20R are sterane compounds measured using *m/z* 217 chromatogram. Pregnane stands for 5α,14β,17β(H)-pregnane, and homopregnane refers to 5α,14β,17β(H)-homopregnane. C27, C28, and C29 ααα 20R are the abbreviations of 20R-5α(H),14α(H),17α(H)-cholestane, 20R-24-methyl-5a(h),14a(h),17a(h)-cholestane, and 20R-24-ethyl-5α(h),14α(h),17α(h)-cholestane, respectively. Relative pregnane content = (pregnane + homopregnane)/C27–C29 ααα sterane.

act as the major nuclei in sandstone reservoirs (McBride, 1989; Goldstein and Rossi, 2002; Worden et al., 2012; Buckley et al., 2018). However, in lacustrine shales lacking siliceous organisms, a large amount of authigenic quartz precipitation has been questioned because of the limitation of nucleation sites and growth space (Dove et al., 2005; Lander et al., 2008). In this study, we found that siliceous resting cysts of algae can play a significant role in silica nucleation, although they are only several nanometers in thickness. According to the SEM-CL analysis, authigenic quartz in the ORL of the shales formed in two stages. One stage shows dark rings several nanometers in thickness, and the other is a light luminescence color and quartz has precipitated over both sides of the dark rings (Figure 12A1, A2). The CL spectrum of the dark rings is characterized by a unimodal distribution with an emission band at approximately 425 nm (Figure 12B1, B2), which is related to intrinsic lattice defects, typically representing a signature for quartz recrystallization (Richter et al., 2003). In the Yanchang Formation organic-rich shales, chrysophytes with siliceous structures were identified as the major organic material by Zhang et al. (2016). Chrysophytes produce siliceous resting cysts, and once the cysts sink to the water bottom, their siliceous walls are well preserved in sediments (Zeeb and Smol, 2001; Zhang et al., 2016). These siliceous cysts can recrystallize into biogenic silica shells at a relatively low temperature of approximately 50°C (Vagle et al., 1994; Worden et al., 2012). The occurrence of the CL spectrum 425 nm peak after silica recrystallization indicates a biogenic source of the dark silica rings (Richter et al., 2003), which is also supported by the algal semblable shapes in SEM-CL images (Figure 12A1, A2; Hansen, 1996). Therefore, in organic-rich areas, algal blooms and large numbers of siliceous cysts were preserved to provide sufficient nuclei for further authigenic quartz precipitation. Authigenic quartz growth, however, has been limited due to the lack of biogenic silica nucleation in organic-poor areas (Figure 3E). The petrographic evidence is that authigenic quartz distribution in the ORL is mainly related to organic matter (Figure 3A–E), and only a few authigenic quartz grains developed in organic-poor areas (Figure 3E). This strongly supports that large amounts of authigenic quartz growth must first and foremost be based on nucleation sites. The recrystallization of siliceous resting cysts of algae can apparently act as perfect nuclei in lacustrine organic-rich shales.

Lamina-Scale Diagenetic Mass Transfer and Organic–Inorganic Interactions

When biogenic silica nucleation sites are preserved in organic-rich areas, the precipitation of light luminescence–colored authigenic quartz must be controlled by other silica sources as well as growth spaces. The buried shales are usually thought to be relatively closed diagenetic systems; thus, large-scale fluid flow and mass transfer are unlikely to occur (Thyberg and Jahren, 2011; Bjørlykke and Jahren, 2012). In this case, microscale diagenetic mass transfer analysis is important for understanding the precipitation of authigenic minerals and the formation of dissolution pores in shales.

Formation of Shale Laminae Fracture and Diagenetic Fluid Activity

According to in situ LA-ICP-MS element analysis of clay agglomerates in the ORL of the Yanchang Formation organic-rich shales, the chondrite-normalized patterns of REE and stable element distribution are very similar to the volcanic rocks in the Qinling provenance (Figure 13A–C), indicating that the parent rocks of clay agglomerates in the ORL were mainly sourced from volcanic materials. The slightly positive anomalies of trace elements As, Sr, and U and the negative anomalies of Cr, Zr, and Hf (Figure 5A) also suggest a volcanic source for smectite (Zhang et al., 2017). In the SFL, some K-feldspars are characterized as rod-like or sharp-angled grains, and the inactive element ratios of Cr/Hf, Cr/Ta and Co/Ni vary in the range of 0.44 to 8.88, 3.42 to 45.13, and 0.19 to 1.31, showing the source of the pyroclasts (Lin et al., 2023). During burial processes, volcanic materials can easily hydrolyze to smectite (Shoval, 2004; Sample et al., 2017). Smectite is thermodynamically unstable with increasing temperatures and quickly transforms into ordered mixed-layer illite-smectite or discrete illite via random mixed-layer illite-smectite (Lynch et al., 1997; Cama et al., 2000; Metwally and Chesnokov, 2012). In the ORL of the Yanchang Formation organic-rich shales, illite and ordered mixed-layer illite-smectite are the major clay mineral types (Figure 2C; Table 1). Smectite is mostly transformed into illite or ordered mixed-layer illite-smectite, as revealed by SEM and XRD analyses (Figures 7B, 8). The lamellar or foliaceous appearance of illite also indicates its smectite precursor (Figure 7A).

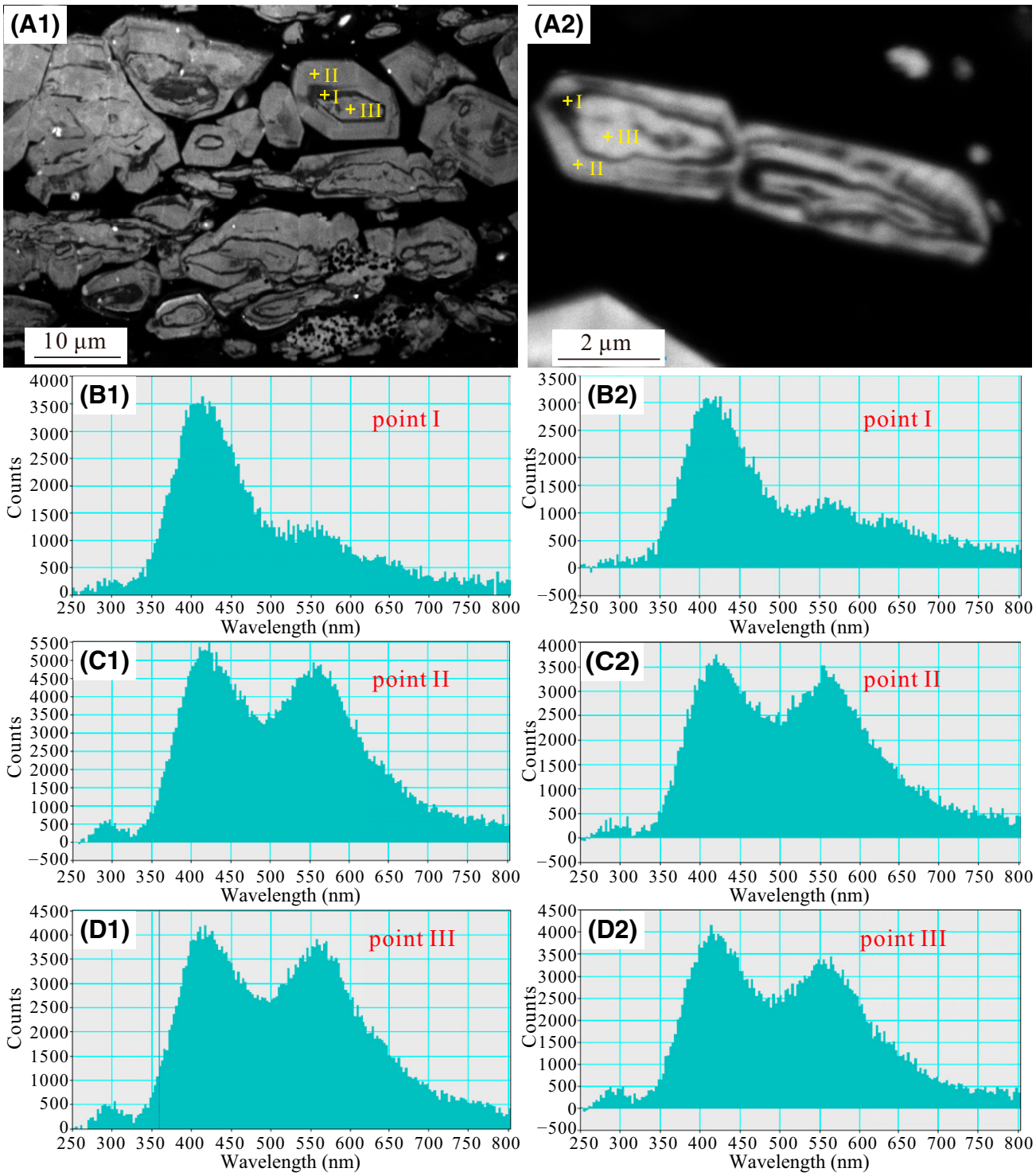

Figure 12. The scanning electron microscopy-cathodoluminescence (SEM-CL) analysis of authigenic quartz in the Yanchang Formation organic-rich shales. (A1, A2) The SEM-CL images showing two generations of authigenic quartz growth, Cai 30, 1964.88 m (6446.46 ft). (B1, B2) The dark rings show unimodal distribution with emission band at approximately 425 nm (1.39×10^{-6} ft) peak. (C1–D2) The CL spectrum of the light luminescence–colored authigenic quartz over dark rings showing bimodal distribution with emission band at approximately 425 nm (1.39×10^{-6} ft) and 580 nm (1.9×10^{-6} ft) peaks.

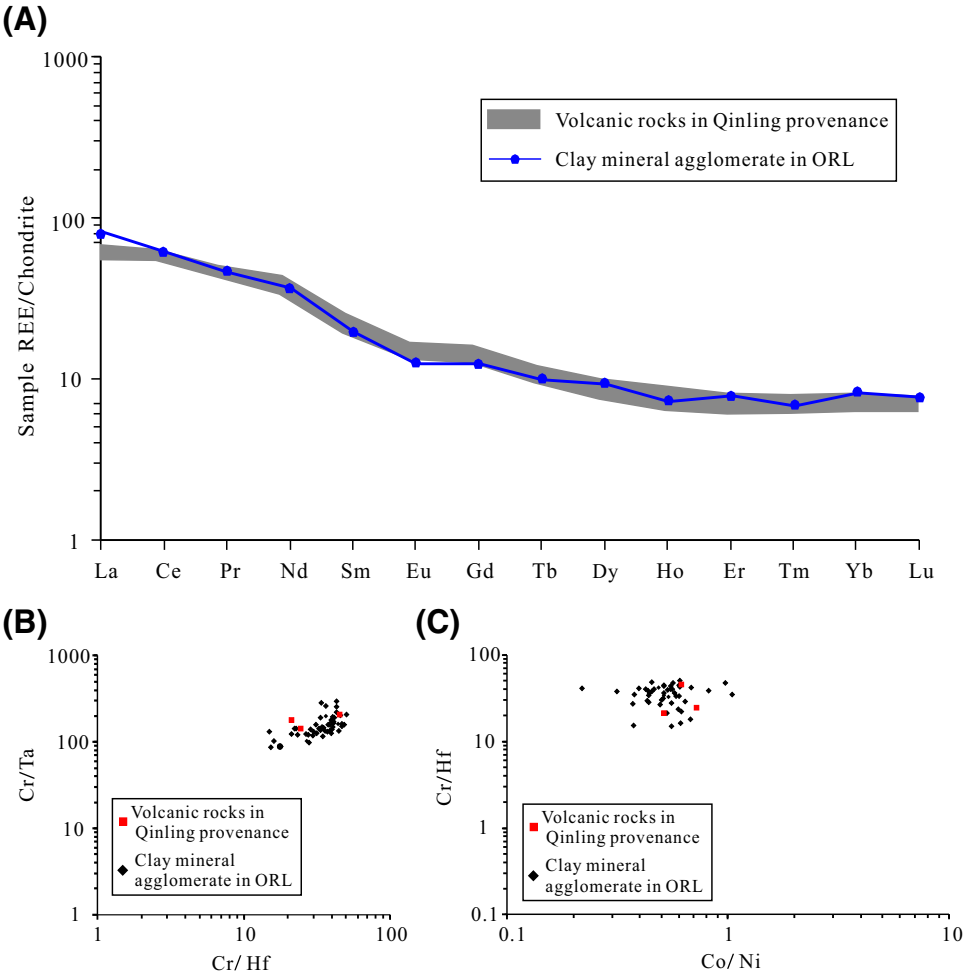

Figure 13. In situ element geochemistry analysis of the organic-rich lamina (ORL) in the Yanchang Formation organic-rich shales. (A) The North American shale composites normalized rare earth element (REE) patterns in the ORL. (B, C) The stable trace element distribution in the ORL. The analysis results showed that parent rocks of clay agglomerates in the ORL mainly sourced from volcanic materials of the Qinling provenance. The element analysis data of volcanic rocks in the Qinling provenance were adapted from Li et al., 2019.

Previous studies have proven that at temperatures of approximately 60°C to 80°C, the loss of water from collapsing clay structures during the transformation of smectite to illite can produce abnormal fluid pressure, causing overpressure in low-permeability shale (Colten-Bradley, 1987; Freed and Peacor, 1989). Moreover, the average bitumen reflectance value in the ORL has been measured at 0.96% (Xi et al., 2020), and hydrocarbon generation can also enhance overpressure under this condition (Wang et al., 2020). In the Triassic Yanchang Formation shales, the overpressure is supported by petrographic evidence of overpressure-induced microfractures in the shale laminae (Figure 14A, B). Overpressure can break the shale structure and open fractures along the laminae interfaces (Jin et al., 2011; Li et al., 2016). Nanoindentation testing shows that the elastic modulus and hardness are anisotropic in the organic-rich shales (Figure 14C). Both elastic modulus and hardness are relatively higher inside the illite agglomerate than along the contact interface of the illite agglomerate and organic matter (Figure 14C). Under this condition, overpressure-induced microfractures can easily occur between clay agglomerates and organic matter stripes (Figure 4C, D). In turn, the fracture opening process releases fluid pressure, which facilitates further transformation of smectite to illite in shales (Freed and Peacor, 1989). After the repetitive pressurization and release process, considerable amounts of microfractures are preserved between the illite agglomerates and organic matter stripes, providing effective spaces for diagenetic fluid flow and authigenic mineral precipitation. This is well

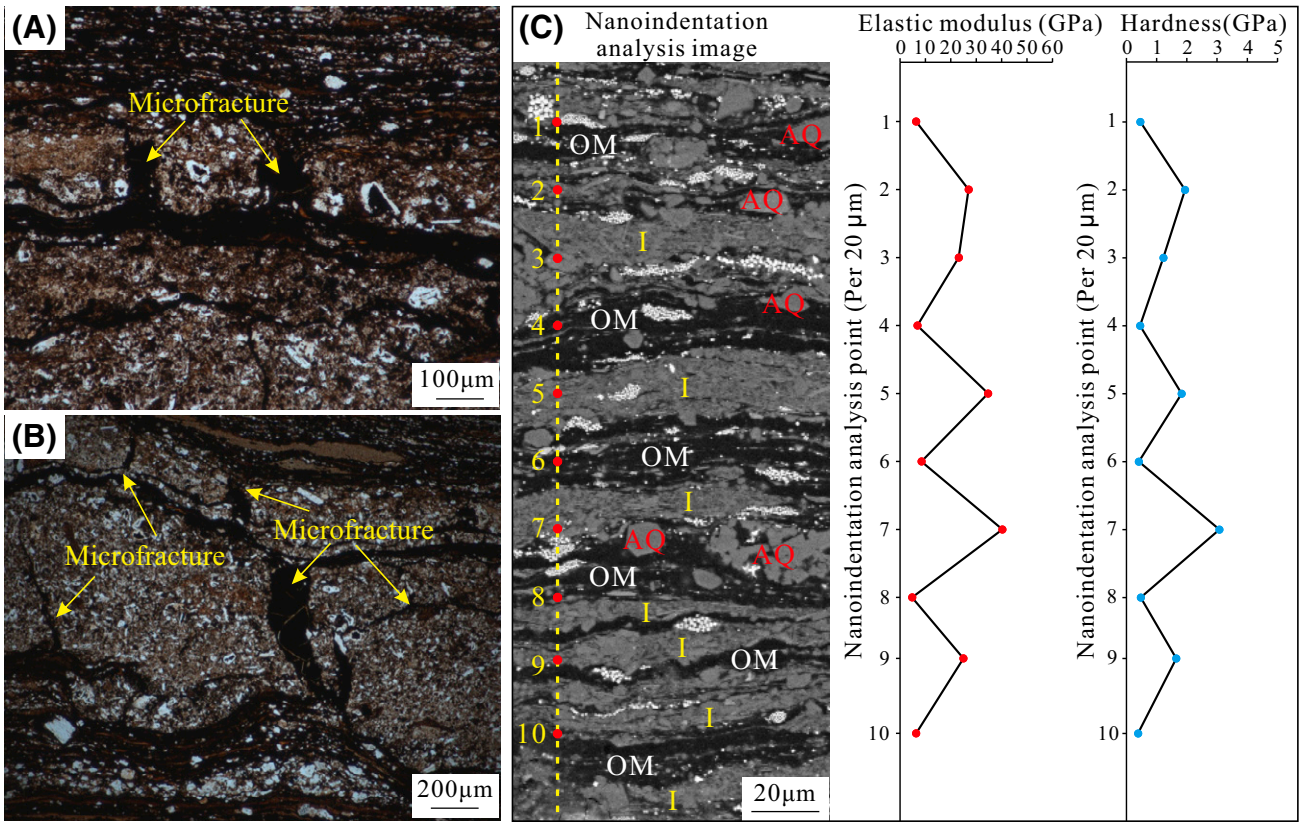

Figure 14. (A, B) The overpressure microfractures in the shale laminae, Ning 70, 1720.7 m (5645.34 ft). (C) Nanoindentation analysis on elastic modulus and hardness in the Yanchang Formation organic-rich shales, Cai 30, 1964.88 m (6446.46 ft). It shows that the modulus and hardness values are relatively lower along the interface of clay agglomerate and organic matter stripe. AQ = authigenic quartz; I = illite; OM = organic matter.

supported by the occurrence of authigenic quartz partly or completely filling the fractures between the clay agglomerates and organic matter (Figure 4C, D).

Lamina-Scale Mass Transfer and Diagenetic Alterations

The smectite-to-illite transformation is the most significant silicate mineral reaction in shales (Awwiller, 1993; Land et al., 1997), especially in lacustrine shales enriched in volcanic material. Petrographic observation and XRD analysis demonstrated the frequent occurrence of smectite-to-illite reactions in the Yanchang Formation organic-rich shales (Figures 7, 8). The clay mineral evolution with respect to burial depth indicates that the smectite-to-illite reaction is clay conservative in the studied shales (Figure 8), which can be exemplified using the equation by Hower et al. (1976):

$$K^+ + Al^{3+} + \text{Smectite} \rightarrow \text{Illite} + Na^+ + Ca^{2+} + Fe^{2+} + Mg^{2+} + Si^{4+} + H_2O \quad (2)$$

This reaction is nearly mass balanced, and Si^{4+} precipitates as authigenic quartz (Awwiller, 1993; Metwally and Chesnokov, 2012). In addition to the 425-nm peak representing silica recrystallization, the CL spectrum of light luminescence–colored authigenic quartz shows an evident 580 nm peak (Figure 12C1, C2, D1, D2), which is caused by intrinsic lattice faults formed during the smectite-to-illite reaction (Thyberg et al., 2010). Microquartz crystals are also observed in the intercrystal pores of the lamelliform or foliaceous illite (Figure 7A). Accordingly, the smectite-to-illite reaction acts as a major silica source for authigenic quartz precipitation. The smectite-to-illite reaction (equation 2) involves K^+, Al^{3+}, Na^+, Fe^{2+}, and Ca^{2+} in the reactant or by-product, which are inevitably mixed into diagenetic fluids and may influence the compounds of authigenic quartz (Xi et al., 2015). According to the in situ LA-ICP-MS element analysis, the authigenic

quartz is rich in Al^{3+} and Fe^{2+}, and trace amounts of K^+, Na^+, and Ca^{2+} are detected, providing indirect evidence for the smectite-to-illite reaction as a silica source for authigenic quartz precipitation in the Yanchang Formation organic-rich shales.

For the smectite-to-illite reaction to proceed continuously toward the right, a source for K^+ is required (equation 2). Therefore, this reaction is commonly associated with K-feldspar albitization or dissolution in sandstone reservoirs (Hower et al., 1976; Bjørlykke and Egeberg, 1993; Worden and Morad, 2000; Xi et al., 2015). However, in shales with extremely low porosity and permeability, the source of K^+ has been debated for a long time. Whether the shale system is closed and K^+ is generated in situ or the shale system is open and K^+ migrates from the surrounding formations is a controversial topic (Weaver and Beck, 1971; Peltonen et al., 2009; Metwally and Chesnokov, 2012; Jin et al., 2013). Previous studies have proven that there is only a small amount of K-feldspar dissolution in the interbedded sandstones, so it is difficult to provide enough K^+ for the smectite-to-illite reaction in the relatively thick shale (Xi et al., 2021). Our data indicate a lamina-scale open system that allows diagenetic mass transfer between the SFL and ORL.

As the burial temperature increased to approximately 60°C, the smectite in the ORL began to transform into illite (Hower et al., 1976; Peltonen et al., 2009). During this reaction, microfractures between clay agglomerates and organic matter could open due to overpressure accumulation and release (Figure 14). Then, the silica sourced from the smectite-to-illite reaction precipitated as authigenic quartz in organic-rich areas along the microfractures, where biogenic silica nucleation existed (Figures 4, 12). Meanwhile, the organic matter in the ORL generated organic acids during the thermal maturation process (Surdam et al., 1989). According to the microdrilling analysis of organic geochemistry, the organic-poor SFL contains more O_2–O_5 compounds than the ORL (Figure 10; Table 2), confirming that organic acids migrated from the ORL to the SFL. Moreover, the expulsion of organic acid from the ORL to the SFL can facilitate further thermal evolution of acidic material in oil (Ma et al., 2022).

In addition to organic acids, evolution of hydrocarbon content in oil is affected by the expulsion process. This process can be supported by the profile of the molecular parameters (Figure 11). The $\sum C_{21-}/\sum C_{22+}$, Ts/hopane, and relative pregnane contents in the lower SFL-rich shale interval are generally greater than those in the upper SFL-poor shale interval (Figure 11). According to the chemical mechanism, the above parameter-related compounds follow the precursor-product relationship and, to be precise, side-chain scission reactions. Specifically, low-molecular-weight n-alkanes can be generated by the thermal cracking of high-molecular-weight n-alkanes (Hill et al., 2003). The Ts is believed to be generated by the cleavage of the side chain of C_{29} and higher-carbon-number hopanoids (Volkman et al., 1983), and pregnane and homopregnane have been shown to result from side-chain cleavage of regular steranes (Huang et al., 1994). In fact, the sample set covered a narrow depth range of less than 15 m, and the thermal maturity of oil was supposed to show very little difference. However, the trend is that the three parameters of shale in the lower SFL-rich interval are greater than those in the upper SFL-poor interval. This may indicate that the expulsion of oil promotes its further thermal cracking reaction (Figure 11).

When organic acids entered the SFL, K-feldspars dissolved (Figure 9A–D). Moreover, the smectite-to-illite reaction would lower the pH of the formation water (Metwally and Chesnokov, 2012), facilitating K-feldspar dissolution. This reaction generates aqueous silica and K^+, which can be expressed as (Bjørlykke and Jahren, 2012)

$$\begin{aligned} KAlSi_3O_8(K-\text{feldspar}) + H^+ + 0.5H_2O \\ = 0.5\ Al_2Si_2O_5(OH)_4(\text{kaolinite}) \\ + 2\ SiO_2(aq) + K^+ \end{aligned} \quad (3)$$

Aqueous silica and K^+ diffused from the SFL to the ORL. The energy spectrum scanning showed that the concentrations of K and Si were high along the interface of the SFL and ORL, and decreased with increasing distance from the SFL (Figure 15A, B). After the aqueous silica and K^+ were released from the SFL, K-feldspar continued to dissolve and produced more K^+. The aqueous silica could precipitate as authigenic quartz in the overpressure-induced microfractures, together with silica sourced from the smectite-to-illite reaction. Meanwhile, K^+ diffusion provided a reactant to the smectite-to-illite reaction

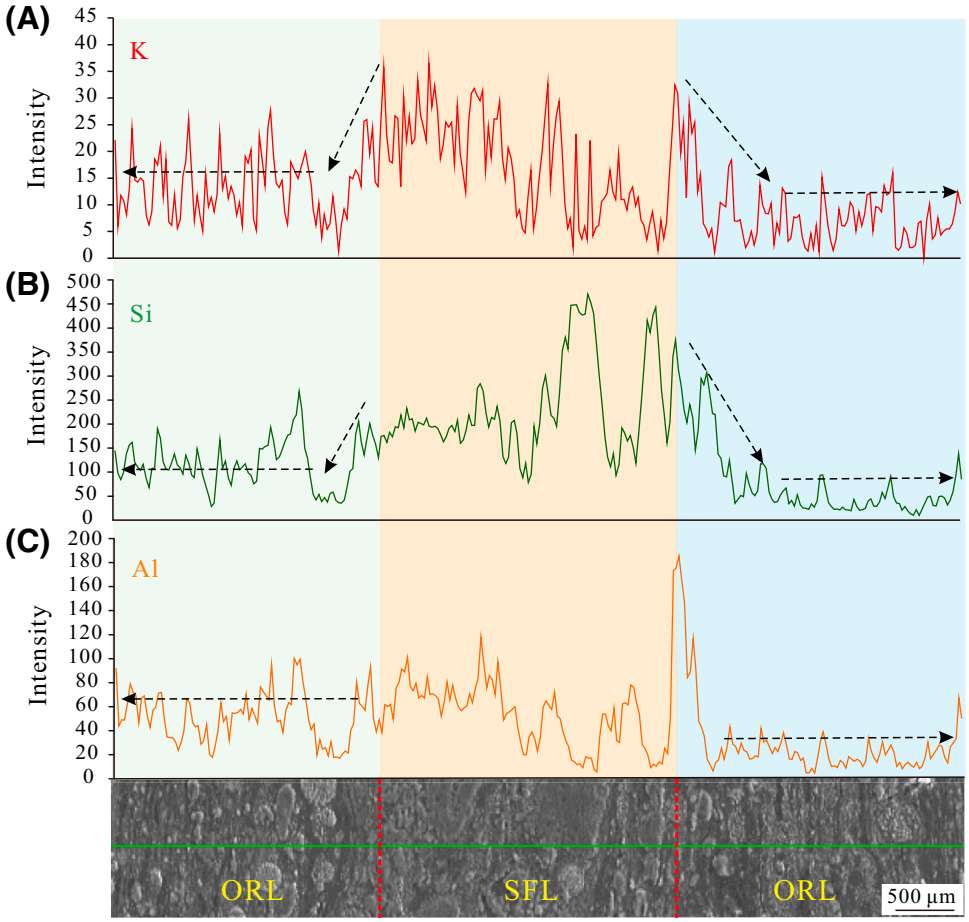

Figure 15. Energy spectrum scanning of K and Si in the direction perpendicular to laminae, Cai 30, 1964.88 m (6446.46 ft), showing that K and Si have migrated from the silt-sized felsic lamina (SFL) to the organic-rich lamina (ORL) in the Yanchang Formation organic-rich shale.

(equation 2) in the ORL. Thus, the smectite-to-illite transformation continuously occurred, generating abnormal fluid pressure and producing more silica. The microfracture opening process generally releases overpressure to a certain extent (Shaw and Primmer, 1989; Hao et al., 1998; Li et al., 2016), promoting the flow of diagenetic fluids. Then, the silica diffused to the microfractures and precipitated over the biogenic silica nuclei on the organic-rich side (Figures 3, 4). Each biogenic silica nucleus controls lenticular microcrystals and aggregates to form an authigenic quartz band in the ORL (Figure 4A, B).

According to micrographic observations and AMICS analysis, the authigenic quartz in the ORL is centered mainly at the position adjoining the SFL (Figures 2C; 3A, B, D), indicating that authigenic quartz precipitation was related to K-feldspar dissolution. Authigenic quartz significantly decreased in the ORL, where fractures developed between the SFL and the ORL (Figure 3C). The reason may be that the K^+ sourced from K-feldspar dissolution just escaped along microfractures between the ORL and SFL and did not effectively enter the ORL. In this case, the smectite-to-illite reaction in the ORL would be limited and may not have produced enough silica for authigenic quartz precipitation. The content of authigenic quartz would, as observed, decrease with increasing distance to the SFL (Figure 3D). This further demonstrates the close genetic relationship between authigenic quartz formation and K-feldspar dissolution. In situ laser Raman spectroscopy analysis shows that the intensity of the Si-O-Si bond in the clay mineral agglomerate decreases from point II to point I in the ORL (Figure 16A, B), which indicates that the degree of smectite-to-illite transformation has increased with decreasing distance from the SFL (Al-Ani and Sarapää, 2008; Kloprogge, 2017). This is because the concentration of K^+ generated by

K-feldspar dissolution was sufficient to drive the smectite-to-illite reaction in point I, and K^+ diffusion decreased with increasing distance to the SFL. The peak value of approximately 464 cm^{-1} in the authigenic quartz Raman spectrum is higher in point III than in point IV (Figure 16C, D), suggesting a higher degree of crystallinity of authigenic quartz close to SFL (Champagnon et al., 1996; Arguirov et al., 2007). This may also be influenced by the degree of smectite-to-illite reaction under different diffusion concentrations of K^+ sourced from SFL (Peltonen et al., 2009; Thyberg et al., 2010). All of the above petrographic evidence supports the fact that diagenetic mass transfer occurred between the ORL and SFL at the microscale, resulting in authigenic quartz precipitation and K-feldspar dissolution in the organic-rich shales.

The K and Si tested by energy spectrum scanning mainly appeared approximately 400 to 500 μm away from the SFL laminae (Figure 15A, B), and the position of occurrence is consistent with authigenic quartz growth (Figures 3C; 4A, C, D). This indicates that mass transfer from the SFL to the ORL significantly controlled the formation of authigenic quartz. When the distance from the SFL is greater than 400 to 500 μm, the concentrations of K and Si in the ORL are low (Figure 15A, B). The concentration of authigenic quartz also decreases (Figures 3C; 4A, C, D) because the smectite-to-illite reaction has been limited by the lack of K^+ diffusion. The concentration

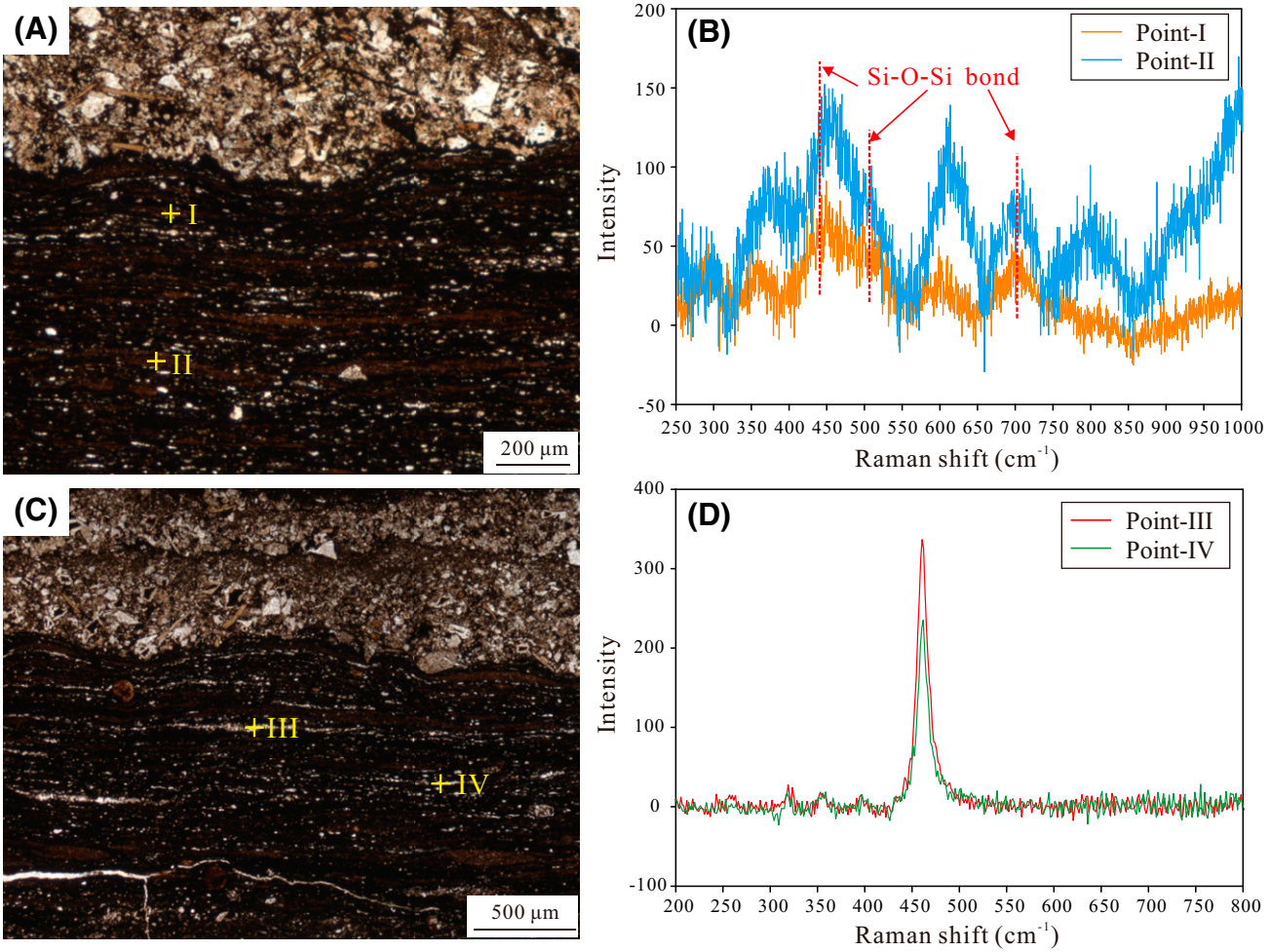

Figure 16. In situ spectroscopy analysis on clay agglomerate and authigenic quartz in the organic-rich lamina with different distance to the silt-sized felsic lamina (SFL) in the Yanchang Formation organic-rich shales. (A, B) The laser Raman spectrum of the clay agglomerate showing increased transformation degree of smectite to illite with decreasing distance to the SFL, Cai 30, 1959.48 m (6428.74 ft). (C, D) The laser Raman spectrum of the authigenic quartz showing increase crystallinity degree with decreasing distance to the SFL, Cai 30, 1964.88 m (6446.46 ft).

of Al shows insignificant variation inside the ORL, but it is high along the interface of SFL and ORL (Figure 15C). This is because kaolinite generated from K-feldspar dissolution mainly distributes along the laminae interface or fills in the dissolution pores of the SFL (Figure 9C, D). Thus, the Al ion is locally conserved in the solids, and does not migrate to any extent between different laminae. In addition, the low overall concentrations of REEs and the uniform distribution of REE patterns in authigenic quartz (Figure 5B) indicate that diagenetic fluid flow in the organic-rich shale only occurred inside the shale systems and was not disturbed by surrounding formations (Phan et al., 2018). The dissolution of volcanic-sourced smectite also released metallic ions into the solution, such as Ca^{2+}, Fe^{2+}, and Mg^{2+}. In the ORL, the concentrations of Ca^{2+} and Mg^{2+} are low, whereas that of Fe^{2+} is high. The scattered euhedral pyrite always develops around authigenic quartz or is accompanied by some lamellar illite (Figure 6A, C, D), indicating that the higher availability of reactive Fe for pyrite formation was supplied by smectite dissolution. The octahedral or pyritohedral shapes of pyrite (Figure 6C, D) and the higher in situ $\delta^{34}S$ values than framboidal pyrite (Figure 6E, F) further supported its diagenetic formation mechanisms related to organic thermal evolution (Siedenberg et al., 2018). During these reactions, the Fe^{2+} was intensively consumed by pyrite precipitation. As a result, the smectite-to-chlorite reaction was inhibited due to lacking Fe^{2+}, which is supported by chlorite content variation trends with respect to burial depth. Thus, we can confirm the conclusions that shale performs mainly as a closed system at the burial diagenetic stages, and the surrounding diagenetic mass is extremely difficult to migrate into the shale formation. Nevertheless, inside the shale formation, a microscale open system exists between the laminae consisting of different compositions, which is significant for lamina-scale mass transfer and by-product redistribution during organic–inorganic interactions.

The Impacts on Shale Oil Reservoir Formation

During the burial process of organic-rich shales, organic matter thermal evolution and inorganic mineral diagenetic alteration occur, resulting in the organic–inorganic interactions summarized in Figure 17. Below a temperature of approximately 60°C, the organic matter is not mature; thus, inorganic mineral diagenesis is the dominant diagenetic reaction in shale formations (Surdam et al., 1989). At this stage, the smectite altered from volcanic materials transformed into ordered mixed-layer illite-smectite and illite and induced overpressure microfractures between clay mineral agglomerates and organic matter. The siliceous resting cysts of algae in the organic-rich areas recrystallized to biogenic silica shells, forming quartz nuclei for further authigenic quartz precipitation (Figure 18). When the temperature increased to higher than 60°C to 70°C, the interactions among mineral dissolution, precipitation, and organic matter decomposition were intense. The smectite-to-illite reaction occurred intensively, generating the major source of authigenic quartz in the ORL. Simultaneously, organic acids were generated from the thermal evolution of organic matter and released to adjoining the SFL. Both processes could induce an acidic environment favorable for authigenic quartz precipitation. However, organic acids caused K-feldspar dissolution when they entered the SFL. During these processes, the mass transfer of K and Si occurred between the SFL and ORL due to the lamina-scale open system, leading to continuous transformation of smectite to illite and precipitation of authigenic quartz over biogenic silica nuclei along the microfractures. As K and Si effectively migrated from the SFL to the ORL, K-feldspar dissolution was promoted, which generated massive formation of secondary pores in the SFL (Figures 9, 18). Subsequently, the dissolution pores are preserved in the shale formation and provide effective spaces for oil storage. The thin section and SEM observations show that most of the K-feldspar dissolution pores were filled with crude oil (Figure 9A–D). The results of organic extraction and Rock-Eval analyses of the microdrilling samples showed that the n-alkane distribution characteristics were similar in the ORL and SFL (Figure 10), implying that the oil in the K-feldspar dissolution pores of the SFL migrated from the ORL (Figure 18). The *EOM*, S_1/*TOC*, *EOM*/*TOC*, and saturated hydrocarbon analyses further confirmed that free hydrocarbons with light n-alkanes migrated from the ORL to the adjoining SFL (Figure 10; Table 3), which was also supported by in situ infrared spectroscopy and laser Raman spectroscopy analyses (Xi et al., 2020). Therefore,

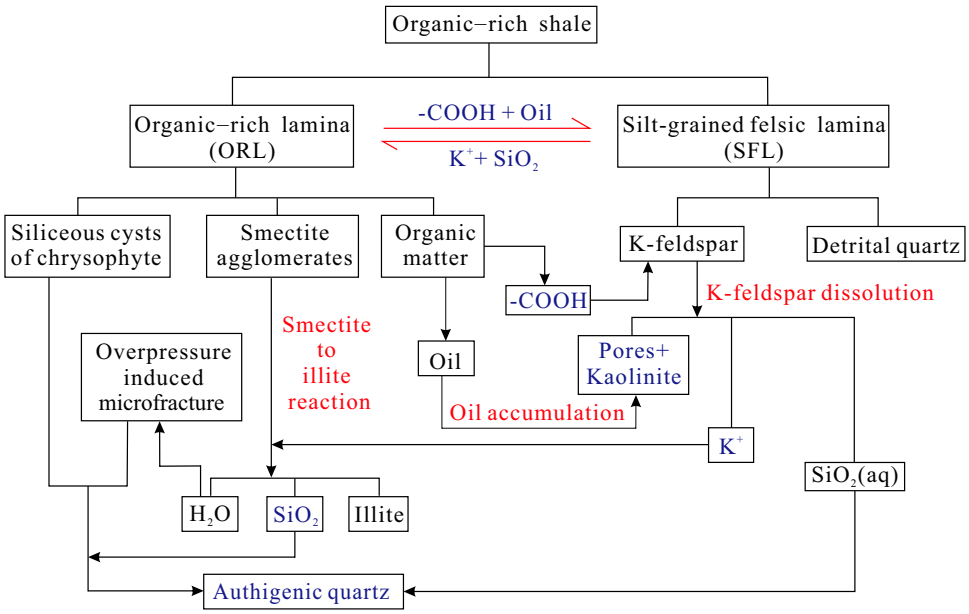

Figure 17. Organic–inorganic interactions and diagenetic mass transfer in the organic-rich shale formation.

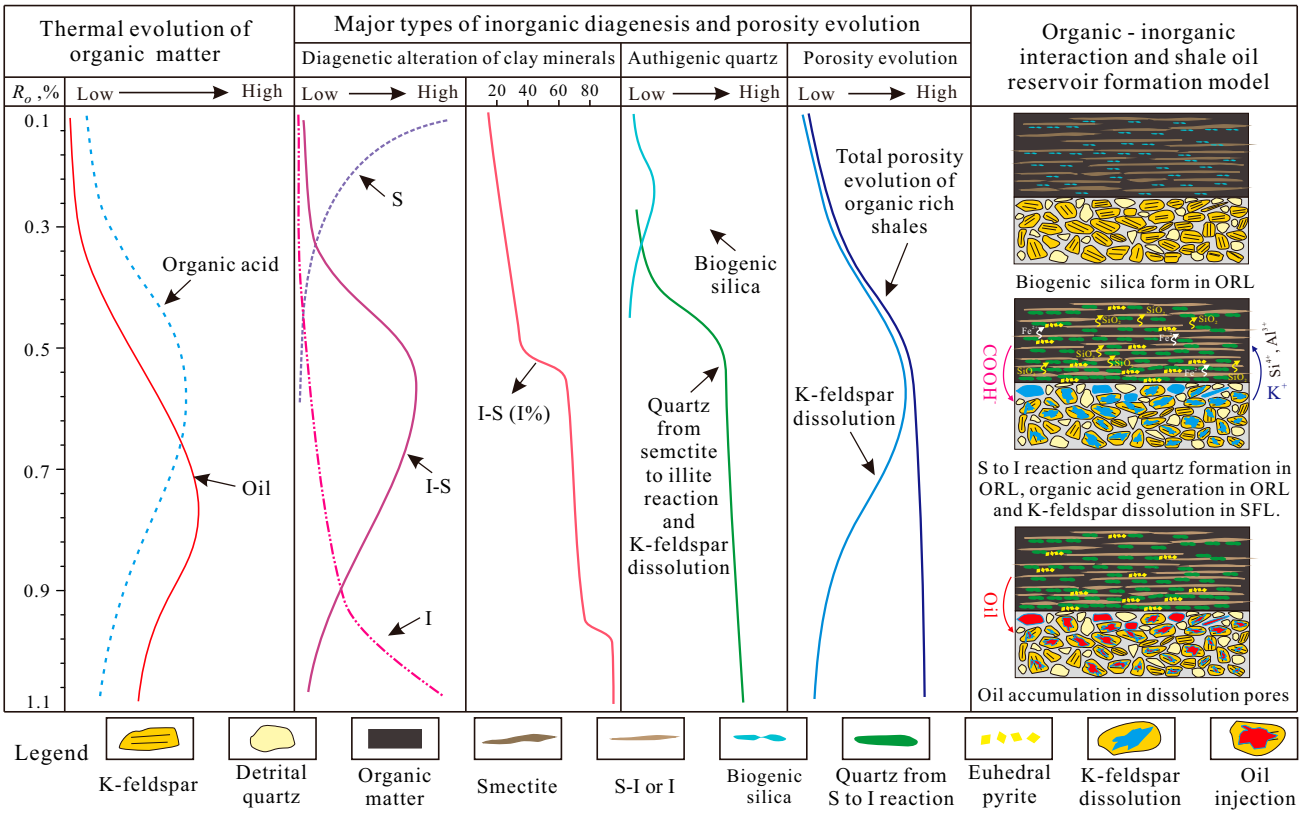

Figure 18. The model of organic–inorganic interaction and shale oil reservoir formation in the organic-rich shales. I = illite; ORL = organic-rich lamina; R_o = vitrinite reflectance; S = smectite; SFL = silt-sized felsic lamina.

the oil generated in the ORL can accumulate preferentially into the K-feldspar dissolution pores in the SFL, resulting in an approximately in situ accumulation (Figure 18), forming favorable shale oil exploration targets. It is also worth noting that authigenic quartz precipitation along the microfractures between clay mineral agglomerates and organic matter can strongly strengthen the brittleness of the ORL in shales (Milliken and Day Stirrat, 2013; Dong et al., 2017; Milliken and Olson, 2017), making shale oil fracturing development more efficient.

CONCLUSIONS

The organic-rich shales in the Yanchang Formation consist mainly of ORL and SFL. Authigenic quartz is the dominant diagenetic mineral type in ORL, whereas K-feldspars are extensively dissolved in SFL. Siliceous nucleation sites are essential for authigenic quartz precipitation. The recrystallization of siliceous resting cysts of algal species can act as perfect silica nuclei in lacustrine organic-rich shale, controlling the occurrence and distribution of authigenic quartz. Authigenic quartz growth in ORL is significantly related to K-feldspar dissolution in SFL. Smectite-to-illite conversion provides the major silica source for authigenic quartz in ORL, and the required K^+ is migrated from adjacent SFL. The lamina-scale open diagenetic system can facilitate diagenetic fluid flow and mass transfer at the microscale within shales. Lamina-scale diagenetic mass transfer enables authigenic mineral precipitation and detrital grain dissolution in a mass balance shale system. Lamina-scale diagenetic mass transfer and material redistribution are key controlling factors for effective pore space formation within a closed shale diagenetic system. Oil generated in ORL can preferentially accumulate in the K-feldspar dissolution pores in SFL.

REFERENCES CITED

Al-Ani, T., and O. Sarapää, 2008, Clay and clay mineralogy: Physical – chemical properties and industrial uses: Espoo, Finland, Geological Survey of Finland M19/3232/2008/41, 96 p.

Arguirov, T., T. Mchedlidze, V. D. Akhmetov, S. Kouteva-Arguirova, M. Kittler, R. Rolver, M. Berghoff, M. Forst, D. L. Batzner, and B. Spangenberg, 2007, Effect of laser annealing on crystallinity of the Si layers in Si/SiO_2 multiple quantum wells: Applied Surface Science, v. 254, no. 4, p. 1083–1086, doi:10.1016/j.apsusc.2007.07.150.

Awwiller, D. N., 1993, Illite/smectite formation and potassium mass transfer during diagenesis of mudrocks: A study from the Texas Gulf Coast Paleocene-Eocene: Journal of Sedimentary Petrology, v. 63, no. 3, p. 501–512.

Bao, Z. A., L. Chen, C. Zong, H. Yuan, K. Chen, and M. Da, 2017, Development of pressed sulfide powder tablets for in situ sulfur and lead isotope measurement using LA-MC-ICP-MS: International Journal of Mass Spectrometry, v. 421, p. 255–262, doi:10.1016/j.ijms.2017.07.015.

Baruch, E. T., M. J. Kennedy, S. C. Löhr, and D. N. Dewhurst, 2015, Feldspar dissolution-enhanced porosity in Paleoproterozoic shale reservoir facies from the Barney Creek Formation: AAPG Bulletin, v. 99, no. 09, p. 1745–1770, doi:10.1306/04061514181.

Berger, G., J. C. Lacharpagne, B. Velde, D. Beaufort, and B. Lanson, 1997, Kinetic constraints on illitization reactions and the effects of organic diagenesis in sandstone/shale sequences: Applied Geochemistry, v. 12, no. 1, p. 23–35, doi:10.1016/S0883-2927(96)00051-0.

Bjørlykke, K., and P. K. Egeberg, 1993, Quartz cementation in sedimentary basins: AAPG Bulletin, v. 77, no. 9, p. 1538–1548.

Bjørlykke, K., and J. Jahren, 2012, Open or closed geochemical systems during diagenesis in sedimentary basins: Constraints on mass transfer during diagenesis and the prediction of porosity in sandstone and carbonate reservoirs: AAPG Bulletin, v. 96, no. 12, p. 2193–2214, doi:10.1306/04301211139.

Boles, J. R., and S. J. Franks, 1979, Clay diagenesis in Wilcox sandstones of south west Texas: Implications of smectite diagenesis on sandstone cementation: Journal of Sedimentary Petrology, v. 49, p. 55–70.

Buckley, P., N. Hargreaves, and S. Cooper, 2018, Nucleation of quartz under ambient conditions: Communications Chemistry, v. 49, no. 1, p. 5327–5331.

Cai, Q., M. Hu, B. Zhang, N. Ngia, A. Liu, R. Liao, O. Kane, et al., 2022, Source of silica and its implications for organic matter enrichment in the Upper Ordovician-Lower Silurian black shale in western Hubei Province, China: Insights from geochemical and petrological analysis: Petroleum Science, v. 19, no. 1, p. 74–90, doi:10.1016/j.petsci.2021.10.012.

Cama, J., J. Ganor, C. Ayora, and A. C. Lasaga, 2000, Smectite dissolution kinetics at 80 °C and pH 8.8: Geochimica et Cosmochimica Acta, v. 64, no. 15, p. 2701–2717, doi:10.1016/S0016-7037(00)00378-1.

Champagnon, B., G. Panczer, C. Chemarin, and B. Humbert-Labeaumaz, 1996, Raman study of quartz amorphization by shock pressure: Journal of Non-Crystalline Solids, v. 196, p. 221–226, doi:10.1016/0022-3093(95)00590-0.

Chen, L., K. Chen, Z. Bao, P. Liang, T. Sun, and H. Yuan, 2017, Preparation of standards for in situ sulfur isotope measurement in sulfide using femtosecond laser ablation MC-ICP-MS: Spectrochimica Acta Part B Atomic Spectroscopy, v. 32, no. 1, p. 107–116.

Colten-Bradley, V. A., 1987, Role of pressure in smectite dehydration—Effects on geopressure and smectite-to-illite transformation: AAPG Bulletin, v. 71, no. 11, p. 1414–1427.

Curtis, C. D., 1978, Possible links between sandstone diagenesis and depth-related geochemical reactions occurring in enclosing mudstones: Journal of the Geological Society, v. 135, no. 1, p. 107–117, doi:10.1144/gsjgs.135.1.0107.

Day-Stirrat, R. J., K. L. Milliken, S. P. Dutton, R. G. Loucks, S. Hillier, A. C. Aplin, and A. M. Schleicher, 2010, Open-system chemical behavior in deep Wilcox group mudstones, Texas Gulf Coast, USA: Marine and Petroleum Geology, v. 27, no. 9, p. 1804–1818, doi:10.1016/j.marpetgeo.2010.08.006.

Dong, T., N. B. Harris, K. Ayranci, and S. Yang, 2017, The impact of rock composition on geomechanical properties of a shale formation: Middle and Upper Devonian Horn River Group shale, Northeast British Columbia, Canada: AAPG Bulletin, v. 101, no. 2, p. 177–204, doi:10.1306/07251615199.

Dove, P. M., N. Han, and J. J. De Yoreo, 2005, Mechanisms of classical crystal growth theory explain quartz and silicate dissolution behavior: Proceedings of the National Academy of Sciences of the United States of America, v. 102, no. 43, p. 15357–15362, doi:10.1073/pnas.0507777102.

Dowey, P. J., and K. Taylor, 2020, Diagenetic mineral development within the Upper Jurassic Haynesville-Bossier Shale, USA: Sedimentology, v. 67, no. 1, p. 47–77, doi:10.1111/sed.12624.

Dowey, P. J., and K. G. Taylor, 2017, Extensive authigenic quartz overgrowths in the gas-bearing Haynesville-Bossier Shale, USA: Sedimentary Geology, v. 356, p. 15–25, doi:10.1016/j.sedgeo.2017.05.001.

Freed, R. L., and D. R. Peacor, 1989, Geopressured shale and sealing effect of smectite to illite transition: AAPG Bulletin, v. 73, no. 10, p. 1223–1232.

Fu, J., W. Guo, S. Li, X. Liu, D. Cheng, and X. Zhou, 2021, Characteristics and exploration potential of muti-type shale oil in the 7th Member of Yanchang Formation, Ordos Basin [in Chinese with English abstract]: Natural Gas Geoscience, v. 32, no. 12, p. 1749–1761.

Fu, J., S. Li, X. Niu, X. Deng, and X. Zhou, 2020, Geological characteristics and exploration of shale oil in Chang 7 Member of Triassic Yanchang Formation, Ordos Basin, NW China: Petroleum Exploration and Development, v. 47, no. 5, p. 931–945, doi:10.1016/S1876-3804(20)60107-0.

Ghanizadeh, A., A. Amann-Hildenbrand, M. Gasparik, Y. Gensterblum, B. M. Krooss, and R. Littke, 2014, Experimental study of fluid transport processes in the matrix system of the European organic-rich shales: II. Posidonia Shale (Lower Toarcian, northern Germany): International Journal of Coal Geology, v. 123, p. 20–33, doi:10.1016/j.coal.2013.06.009.

Goldstein, R. H., and C. Rossi, 2002, Recrystallization in quartz overgrowths: Journal of Sedimentary Research, v. 72, no. 3, p. 432–440, doi:10.1306/110201720432.

Hansen, P., 1996, Silica-scale Chrysophyceae and Synurophyceae from Madagascar: Archiv fur Protistenkunde, v. 147, no. 2, p. 145–172, doi:10.1016/S0003-9365(96)80030-3.

Hao, F., S. Li, W. Dong, Z. Hu, and B. Huang, 1998, Abnormal organic-matter maturation in the Yinggehai Basin, South China Sea: Implications for hydrocarbon expulsion and fluid migration from overpressure systems: Journal of Petroleum Geology, v. 21, no. 4, p. 427–444, doi:10.1111/j.1747-5457.1998.tb00794.x.

Hill, R. J., Y. Tang, and I. R. Kaplan, 2003, Insights into oil cracking based on laboratory experiments: Organic Geochemistry, v. 34, no. 12, p. 1651–1672, doi:10.1016/S0146-6380(03)00173-6.

Hower, J., E. Eslinger, M. E. Hower, and E. A. Perry, 1976, Mechanism of burial metamorphism of argillaceous sediment: 1. Mineralogical and chemical evidence: GSA Bulletin, v. 87, no. 5, p. 725–737, doi:10.1130/0016-7606(1976)87<725:MOBMOA>2.0.CO;2.

Huang, D., D. Zhang, and J. Li, 1994, The origin of 4-methyl steranes and pregnanes from Tertiary strata in the Qaidam Basin, China: Organic Geochemistry, v. 22, no. 2, p. 343–348, doi:10.1016/0146-6380(94)90180-5.

Ilgen, A. C., J. E. Heath, I. Y. Akkutlu, L. T. Bryndzia, D. R. Cole, Y. K. Kharaka, T. J. Kneafsey, K. L. Milliken, L. J. Pyrak-Nolte, and R. Suarez-Rivera, 2017, Shales at all scales: Exploring coupled processes in mudrocks: Earth-Science Reviews, v. 166, p. 132–152, doi:10.1016/j.earscirev.2016.12.013.

Inoue, A., N. Kohyama, R. Kitagawa, and T. Watanabe, 1987, Chemical and morphological evidence for the conversion of smectite to illite: Clays and Clay Minerals, v. 35, no. 2, p. 111–120, doi:10.1346/CCMN.1987.0350203.

Inoue, A., M. Utada, and K. Wakita, 1992, Smectite-to-illite conversion in natural hydrothermal systems: Applied Clay Science, v. 7, no. 1–3, p. 131–145, doi:10.1016/0169-1317(92)90035-L.

Jautzy, J. J., D. C. Petts, I. D. Clark, T. A. Al, R. A. Stern, and M. Jensen, 2020, Diagenetic evolution of a sedimentary system (Michigan Basin): Insights from petrography and S-isotope micro-analysis of pyrite: Chemical Geology, v. 541, 119580, 14 p., doi:10.1016/j.chemgeo.2020.119580.

Ji, L., K. Yan, F. Meng, and M. Zhao, 2010, The oleaginous Botryococcus from the Triassic Yanchang Formation in Ordos Basin, northwestern China: Morphology and its paleoenvironmental significance: Journal of Asian Earth Sciences, v. 38, no. 5, p. 175–185, doi:10.1016/j.jseaes.2009.12.010.

Jia, C., M. Zheng, and Y. Zhang, 2012, Unconventional hydrocarbon resources in China and the prospect of exploration and development: Petroleum Exploration and Development, v. 39, no. 2, p. 139–146, doi:10.1016/S1876-3804(12)60026-3.

Jiang, Z., J. Zhang, X. Kong, H. Xie, H. Cheng, and L. Wang, 2023, Research progress and development direction of continental shale oil and gas deposition and reservoirs in China [in Chinese with English abstract]: Acta Petrolei Sinica, v. 44, no. 1, p. 45–72.

Jin, L., R. Mathur, G. Rother, D. Cole, E. Bazilevskaya, J. Williams, A. Carone, and S. Brantley, 2013, Evolution of porosity and geochemistry in Marcellus Formation black shale during weathering: Chemical Geology, v. 356, p. 50–63, doi:10.1016/j.chemgeo.2013.07.012.

Jin, L., G. Rother, D. R. Cole, D. F. R. Mildner, C. J. Duffy, and S. L. Brantley, 2011, Characterization of deep weathering and nanoporosity development in shale—A neutron study: American Mineralogist, v. 96, no. 4, p. 498–512, doi:10.2138/am.2011.3598.

Jin, Z., R. Zhu, X. Liang, and Y. Shen, 2021, Several issues worthy of attention in current lacustrine shale oil exploration and development: Petroleum Exploration and Development, v. 48, no. 6, p. 1471–1484, doi:10.1016/S1876-3804(21)60303-8.

Khalil, K., C. Rabouille, and M. Gallinari, 2007, Constraining biogenic silica dissolution in marine sediments: A comparison between diagenetic models and experimental dissolution rates: Marine Chemistry, v. 106, no. 1–2, p. 223–238, doi:10.1016/j.marchem.2006.12.004.

Kloprogge, J. T., 2017, Chapter 6 - Raman spectroscopy of clay minerals, *in* W. P. Gates, J. T. Kloprogge, J. Madejová, and F. Bergaya, eds., Infrared and Raman spectroscopies of clay minerals: New York, Elsevier, p. 150–199.

Lai, J., G. Wang, Y. Ran, Z. Zhou, and Y. Cui, 2016, Impact of diagenesis on the reservoir quality of tight oil sandstones: The case of Upper Triassic Yanchang Formation Chang 7 oil layers in Ordos Basin, China: Journal of Petroleum Science Engineering, v. 145, p. 54–65, doi:10.1016/j.petrol.2016.03.009.

Land, L. S., L. E. Mack, K. L. Milliken, and F. L. Lynch, 1997, Burial diagenesis of argillaceous sediment, south Texas Gulf of Mexico sedimentary basin: A reexamination: GSA Bulletin, v. 109, no. 1, p. 2–15, doi:10.1130/0016-7606(1997)109<0002:BDOASS>2.3.CO;2.

Lander, R. H., R. E. Larese, and L. M. Bonnell, 2008, Toward more accurate quartz cement models: The importance of euhedral versus noneuhedral growth rates: AAPG Bulletin, v. 92, no. 11, p. 1537–1563, doi:10.1306/07160808037.

Li, S., Y. Yuan, W. Sun, D. Sun, and Z. Jin, 2016, Formation and destruction mechanism as well as major controlling factors of the Silurian shale gas overpressure in the Sichuan Basin, China: Journal of Natural Gas Geoscience, v. 1, no. 4, p. 287–294, doi:10.1016/j.jnggs.2016.09.002.

Li, Z., X. Zhang, J. Zeng, J. Qi, H. Zhang, and Z. Jin, 2019, The characteristics and geological significance of the Adakite rocks of the upper Triassic stata Huari formation volcanics in west Qinling [in Chinese with English abstract]: Mineral Exploration, v. 10, no. 6, p. 1361–1368.

Lin, M., K. Xi, Y. Cao, K. Liu, and R. Zhu, 2023, Periodic paleo-environment oscillation on multi-timescales in the Triassic and their significant implications for algal blooms: A case study on the lacustrine shales in Ordos Basin: Palaeogeography, Palaeoclimatology, Palaeoecology, v. 612, 111376, 13 p., doi:10.1016/j.palaeo.2022.111376.

Liu, B., H. Wang, X. Fu, Y. Bai, L. Bai, M. Jia, and B. He, 2019, Lithofacies and depositional setting of a highly prospective lacustrine shale oil succession from the Upper Cretaceous Qingshankou Formation in the Gulong sag, northern Songliao Basin, northeast China: AAPG Bulletin, v. 103, no. 2, p. 405–432, doi:10.1306/08031817416.

Liu, B., Y. Wang, S. Tian, Y. Guo, L. Wang, Q. Yasin, and J. Yang, 2022, Impact of thermal maturity on the diagenesis and porosity of lacustrine oil-prone shales: Insights from natural shale samples with thermal maturation in the oil generation window: International Journal of Coal Geology, v. 261, 104079, 14 p., doi:10.1016/j.coal.2022.104079.

Liu, Q., D. Zhu, Q. Meng, J. Liu, X. Wu, B. Zhou, Q. Fu, and Z. Jin, 2018, The scientific connotation of oil and gas formations under deep fluids and organic-inorganic interaction: Science China Earth Sciences, v. 62, no. 3, p. 507–528, doi:10.1007/s11430-018-9281-2.

Liu, Y., S. Gao, Z. Hu, C. Gao, K. Zong, and D. Wang, 2010, Continental and oceanic crust recycling-induced melt-peridotite interactions in the Trans-North China Orogen: U-Pb dating, Hf isotopes and trace elements in zircons of mantle xenoliths: Journal of Petrology, v. 51, no. 1–2, p. 537–571, doi:10.1093/petrology/egp082.

Liu, Y., Z. Hu, S. Gao, D. Günther, J. Xu, C. Gao, and H. Chen, 2008, In situ analysis of major and trace elements of anhydrous minerals by LA-ICP-MS without applying an internal standard: Chemical Geology, v. 257, no. 1–2, p. 34–43, doi:10.1016/j.chemgeo.2008.08.004.

Löhr, S. C., E. T. Baruch, P. A. Hall, and M. J. Kennedy, 2015, Is organic pore development in gas shales influenced by the primary porosity and structure of thermally immature organic matter?: Organic Geochemistry, v. 87, p. 119–132, doi:10.1016/j.orggeochem.2015.07.010.

Loucks, R. G., R. M. Reed, S. C. Ruppel, and U. Hammes, 2012, Spectrum of pore types and networks in mudrocks and a descriptive classification for matrix-related mudrock pores: AAPG Bulletin, v. 96, no. 6, p. 1071–1098, doi:10.1306/08171111061.

Lynch, L. F., E. L. Mack, and S. L. Land, 1997, Burial diagenesis of illite/smectite in shales and the origins of authigenic quartz and secondary porosity in sandstones: Geochimica et Cosmochimica Acta, v. 61, no. 10, p. 1995–2006, doi:10.1016/S0016-7037(97)00066-5.

Ma, W., Y. Cao, K. Xi, K. Liu, M. Lin, and J. Liu, 2022, Interactions between mineral evolution and organic acids dissolved in bitumen in hybrid shale system: International Journal of Coal Geology, v. 260, 104071, 13 p., doi:10.1016/j.coal.2022.104071.

Macquaker, J. H. S., K. G. Taylor, M. Keller, and D. Polya, 2014, Compositional controls on early diagenetic pathways in fine-grained sedimentary rocks: Implications for predicting unconventional reservoir attributes of mudstones: AAPG Bulletin, v. 98, no. 3, p. 587–603, doi:10.1306/08201311176.

McBride, E. F., 1989, Quartz cement in sandstones: A review: Earth-Science Reviews, v. 26, no. 1–3, p. 69–112, doi:10.1016/0012-8252(89)90019-6.

Metwally, Y. M., and E. M. Chesnokov, 2012, Clay mineral transformation as a major source for authigenic quartz in

thermo-mature gas shale: Applied Clay Science, v. 55, p. 138–150, doi:10.1016/j.clay.2011.11.007.
Milliken, K. L., and R. J. Day-Stirrat, 2013, Cementation in mudrocks: Brief review with examples from cratonic basin mudrocks, *in* J. Chatellier and D. Jarvie, eds., Critical assessment of shale resource plays: AAPG Memoir 103, p. 133–150.
Milliken, K. L., S. M. Ergene, and A. Ozkan, 2016, Quartz types, authigenic and detrital, in the Upper Cretaceous Eagle Formation, South Texas, USA: Sedimentary Geology, v. 339, p. 273–288, doi:10.1016/j.sedgeo.2016.03.012.
Milliken, K. L., D. McCarty, and A. Derkowski, 2018, Grain assemblages and diagenesis in the tarl-dominated Lower Silurian mudrock succession of the western margin of the east European craton in Poland and Lithuania: Sedimentary Geology, v. 374, p. 115–133, doi:10.1016/j.sedgeo.2018.07.011.
Milliken, K. L., and T. Olson, 2017, Silica diagenesis, porosity evolution, and mechanical behavior in siliceous mudstones, Mowry shale (Cretaceous), Rocky Mountains, USA: Journal of Sedimentary Research, v. 87, no. 4, p. 366–387, doi:10.2110/jsr.2017.24.
Morad, S., K. Al-Ramadan, J. Ketzer, and L. De Ros, 2010, The impact of diagenesis on the heterogeneity of sandstone reservoirs: A review of the role of depositional facies and sequence stratigraphy: AAPG Bulletin, v. 94, no. 8, p. 1267–1309, doi:10.1306/04211009178.
Morad, S., J. M. Ketzer, and L. F. De Ros, 2000, Spatial and temporal distribution of diagenetic alterations in siliciclastic rocks: Implications for mass transfer in sedimentary basins: Sedimentology, v. 47, Suppl. 1, p. 95–120.
Peltonen, C., Ø. Marcussen, K. Bjørlykke, and J. Jahren, 2009, Clay mineral diagenesis and quartz cementation in mudstones: The effects of smectite to illite reaction on rock properties: Marine and Petroleum Geology, v. 26, no. 6, p. 887–898, doi:10.1016/j.marpetgeo.2008.01.021.
Peng, J., K. Milliken, and Q. Fu, 2020, Quartz types in the Upper Pennsylvanian organic-rich Cline Shale (Wolfcamp D), Midland Basin, Texas: Implications for silica diagenesis, porosity evolution and rock mechanical properties: Sedimentology, v. 67, no. 4, p. 2040–2064, doi:10.1111/sed.12694.
Phan, T. T., J. B. Gardiner, R. C. Capo, and B. W. Stewart, 2018, Geochemical and multi-isotopic ($^{87}Sr/^{86}Sr$, $^{143}Nd/^{144}Nd$, $^{238}U/^{235}U$) perspectives of sediment sources, depositional conditions, and diagenesis of the Marcellus Shale, Appalachian Basin, USA: Geochimica et Cosmochimica Acta, v. 222, p. 187–211, doi:10.1016/j.gca.2017.10.021.
Potter, P. E., J. B. Maynard, and P. J. Depetris, 2005, Mud and mudstones: Introduction and overview: New York, Springer, 297 p., doi:10.1007/b138571
Pradier, B., P. Bertrand, L. Martinez, and F. Laggoun-Defarge, 1991, Fluorescence of organic matter and thermal maturity assessment: Organic Geochemistry, v. 17, no. 4, p. 511–524, doi:10.1016/0146-6380(91)90115-Z.
Richter, D. K., T. Götte, J. Götze, and R. D. Neuser, 2003, Progress in application of cathodoluminescence (CL) in sedimentary petrology: Mineralogy and Petrology, v. 79, no. 3–4, p. 127–166, doi:10.1007/s00710-003-0237-4.
Rickard, D., 2019, How long does it take a pyrite framboid to form?: Earth and Planetary Science Letters, v. 513, p. 64–68, doi:10.1016/j.epsl.2019.02.019.
Rimstidt, J. D., J. A. Chermak, and M. E. Schreiber, 2017, Processes that control mineral and element abundances in shales: Earth-Science Reviews, v. 171, p. 383–399, doi:10.1016/j.earscirev.2017.06.010.
Ross, D. J., and R. M. Bustin, 2008, Characterizing the shale gas resource potential of Devonian–Mississippian strata in the Western Canada sedimentary basin: Application of an integrated formation evaluation: AAPG Bulletin, v. 92, no. 1, p. 87–125, doi:10.1306/09040707048.
Sample, J. C., M. E. Torres, A. Fisher, W. Hong, C. Destrigneville, W. F. Defliese, and A. E. Tripati, 2017, Geochemical constraints on the temperature and timing of carbonate formation and lithification in the Nankai Trough, NanTroSEIZE transect: Geochimica et Cosmochimica Acta, v. 198, p. 92–114, doi:10.1016/j.gca.2016.10.013.
Schieber, J., D. Krinsley, and L. Riciputi, 2000, Diagenetic origin of quartz silt in mudstones and implications for silica cycling: Nature, v. 406, no. 6799, p. 981–985, doi:10.1038/35023143.
Schieber, J., W. Zimmerle, and P. S. Sethi, 1998, Shales and mudstones: Stuttgart, Germany, Schweizerbart'sche Verlagsbuchhandlung, v. I and II, 680 p.
Shaldybin, M. V., Y. M. Lopushnyak, I. V. Goncharov, M. J. Wilson, L. Wilson, and B. G. Mendis, 2017, The mineralogy of the clayey-silty siliceous rocks in the Bazhenov Shale Formation (Upper Jurassic) in the west Siberian Basin, Russia: The role of diagenesis and possible implications for their exploitation as an unconventional hydrocarbon reservoir: Applied Clay Science, v. 136, p. 75–89, doi:10.1016/j.clay.2016.11.009.
Shaw, H. F., and T. J. Primmer, 1989, Diagenesis in shales from a partly overpressured sequence in the Gulf Coast, Texas, USA: Marine and Petroleum Geology, v. 6, no. 2, p. 121–128, doi:10.1016/0264-8172(89)90015-9.
Shoval, S., 2004, Deposition of volcanogenic smectite along the southeastern Neo-Tethys margin during the oceanic convergence stage: Applied Clay Science, v. 24, no. 3–4, p. 299–311, doi:10.1016/j.clay.2003.08.009.
Siedenberg, K., H. Strauss, O. Podlaha, and S. van den Boorn, 2018, Multiple sulfur isotopes ($\delta^{34}S$, $\delta^{33}S$) of organic sulfur and pyrite from Late Cretaceous to Early Eocene oil shales in Jordan: Organic Geochemistry, v. 125, p. 29–40, doi:10.1016/j.orggeochem.2018.08.002.
Stixrude, L., and D. R. Peacor, 2002, First-principles study of illite–smectite and implications for clay mineral systems: Nature, v. 420, no. 6912, p. 165–168, doi:10.1038/nature01155.
Sun, L., W. Zhao, H. Liu, R. Zhu, B. Bai, Y. Kang, J. Zhang, and S. Wu, 2023, Concept and application of "sweet spot" in shale oil [in Chinese with English abstract]: Acta Petrolei Sinica, v. 44, no. 1, p. 1–13.
Sun, N., T. Chen, J. Zhong, J. Gao, X. Shi, C. Xue, and R. Swenned, 2022, Petrographic and geochemical characteristics of deep-lacustrine organic-rich mudstone and

shale of the Upper Triassic Chang 7 member in the southern Ordos Basin, northern China: Implications for shale oil exploration: Journal of Asian Earth Sciences, v. 227, 105118, 19 p., doi:10.1016/j.jseaes.2022.105118.

Surdam, R. C., L. J. Crossey, E. S. Hagen, and H. P. Heasler, 1989, Organic-inorganic and sandstone diagenesis: AAPG Bulletin, v. 73, no. 1, p. 1–23.

Taylor, K. G., and J. H. S. Macquaker, 2014, Diagenetic alterations in a silt- and clay-rich mudstone succession: An example from the Upper Cretaceous Mancos Shale of Utah, USA: Clay Minerals, v. 49, no. 2, p. 213–227, doi:10.1180/claymin.2014.049.2.05.

Taylor, T., M. Giles, L. Hathon, T. Diggs, N. Braunsdorf, G. Birbiglia, M. Kittridge, C. Macaulay, and I. Espejo, 2010, Sandstone diagenesis and reservoir quality prediction: Models, myths, and reality: AAPG Bulletin, v. 94, no. 8, p. 1093–1132, doi:10.1306/04211009123.

Thyberg, B., and J. Jahren, 2011, Quartz cementation in mudstones: Sheet-like quartz cement from clay mineral reactions during burial: Petroleum Geoscience, v. 17, no. 1, p. 53–63, doi:10.1144/1354-079310-028.

Thyberg, B., J. Jahren, T. Winje, K. Bjørlykke, J. I. Faleide, and Ø. Marcusssen, 2010, Quartz cementation in Late Cretaceous mudstones, northern North Sea: Changes in rock properties due to dissolution of smectite and precipitation of micro-quartz crystals: Marine and Petroleum Geology, v. 27, no. 8, p. 1752–1764, doi:10.1016/j.marpetgeo.2009.07.005.

Tomczyk, N. A., R. E. Winans, J. H. Shinn, and R. C. Robinson, 2001, On the nature and origin of acidic species in petroleum. 1. Detailed acid type distribution in a California crude oil: Energy & Fuels, v. 15, no. 6, p. 1498–1504, doi:10.1021/ef010106v.

Vagle, G. B., A. Hurst, and H. Dypvik, 1994, Origin of quartz cement in some sandstone from the Jurassic of the Inner Moray Firth (UK): Sedimentology, v. 41, no. 2, p. 363–377, doi:10.1111/j.1365-3091.1994.tb01411.x.

Van de Kamp, P. C., 2008, Smectite-illite-muscovite transformations, quartz dissolution, and silica release in shales: Clays and Clay Minerals, v. 56, no. 1, p. 66–81, doi:10.1346/CCMN.2008.0560106.

Volkman, J. K., R. Alexander, R. I. Kagi, R. A. Noble, and G. W. Woodhouse, 1983, A geochemical reconstruction of oil generation in the Barrow Sub-basin of Western Australia: Geochimica et Cosmochimica Acta, v. 47, no. 12, p. 2091–2105, doi:10.1016/0016-7037(83)90034-0.

Wang, M., Y. Chen, W. Bain, G. Song, K. Liu, Z. Zhou, and M. Steele-MacInnis, 2020, Direct evidence for fluid overpressure during hydrocarbon generation and expulsion from organic-rich shales: Geology, v. 48, no. 4, p. 374–378, doi:10.1130/G46650.1.

Weaver, C. E., and K. C. Beck, 1971, Clay water diagenesis during burial: How mud becomes gneiss: Boulder, Colorado, Geological Society of America Special Papers 134, 78 p., doi:10.1130/SPE134-p1.

Wilson, M., M. Shaldybin, and L. Wilson, 2016, Clay mineralogy and unconventional hydrocarbon shale reservoirs in the USA. I. Occurrence and interpretation of mixed-layer R3 ordered illite/smectite: Earth-Science Reviews, v. 158, p. 31–50, doi:10.1016/j.earscirev.2016.04.004.

Worden, R. H., M. W. French, and E. Mariani, 2012, Amorphous silica nanofilms result in growth of misoriented microcrystalline quartz cement maintaining porosity in deeply buried sandstones: Geology, v. 40, no. 2, p. 179–182, doi:10.1130/G32661.1.

Worden, R. H., and S. Morad, 2000, Quartz cementation in oil field sandstones: A review of the key controversies, in R. H. Worden and S. Morad, eds., Quartz cementation in sandstones: New York, Wiley, p. 1–20, doi:10.1002/9781444304237.ch1.

Wu, S., Z. Yang, X. Zhai, J. Cui, L. Bai, S. Pan, and J. Cui, 2019, An experimental study of organic matter, minerals and porosity evolution in shales within high-temperature and high-pressure constraints: Marine and Petroleum Geology, v. 102, p. 377–390, doi:10.1016/j.marpetgeo.2018.12.014.

Xi, K., Y. Cao, J. Jaren, R. Zhu, K. Bjørlykke, X. Zhang, L. Cai, and H. Hellevang, 2015, Quartz cement and its origin in tight sandstone reservoirs of the Cretaceous Quantou formation in the southern Songliao Basin, China: Marine and Petroleum Geology, v. 66, Part 4, p. 748–763, doi:10.1016/j.marpetgeo.2015.07.017.

Xi, K., Y. Cao, K. Liu, S. Wu, G. Yuan, R. Zhu, Y. Zhao, and H. Hellevang, 2019, Geochemical constraints on the origins of calcite cements and their impacts on reservoir heterogeneities: A case study on tight oil sandstones of the Upper Triassic Yanchang Formation, southwestern Ordos Basin, China: AAPG Bulletin, v. 103, no. 10, p. 2447–2485, doi:10.1306/01301918093.

Xi, K., K. Li, Y. Cao, M. Lin, X. Niu, R. Zhu, X. Wei, Y. You, X. Liang, and S. Feng, 2020, Laminae combination and shale oil enrichment patterns of Chang 73 sub-member organic-rich shales in the Triassic Yanchang Formation, Ordos Basin, NW China.: Petroleum Exploration and Development, v. 47, no. 6, p. 1342–1353, doi:10.1016/S1876-3804(20)60142-8.

Xi, K., K. Li, Y. Cao, X. Niu, M. Lin, Y. You, and S. Feng, 2021, Synergistic diagenesis of sandstone and mudstone in Chang 7_3 sub-member of Triassic Yanchang Formation in Ordos Basin: Journal of China University of Petroleum, v. 45, no. 12, p. 1–11.

Yang, S., and Q. Yu, 2022, The role of fluid-rock interactions in permeability behavior of shale with different pore fluids: International Journal of Rock Mechanics and Mining Sciences, v. 150, 105023, 15 p., doi:10.1016/j.ijrmms.2021.105023.

Zeeb, B. A., and J. P. Smol, 2001, Chrysophyte scales and cysts, *in* J. P. Smol, W. M. Last, and J. B. Birks, eds., Tracking environmental change using lake sediments: Terrestrial, algal and siliceous indicators: New York, Springer, v. 3, p. 203–223.

Zeng, L., H. Akhondzadeh, M. A. Iqbal, A. Keshavarz, R. Rezaee, and Q. Xie, 2022, Effect of fluid-shale interactions on shales micromechanics: Nanoindentation experiments and interpretation from geochemical perspective: Journal of Natural Gas Science and

Engineering, v. 101, 104545, 11 p., doi:10.1016/j.jngse.2022.104545.

Zhang, W., H. Yang, X. Xia, L. Xie, and G. Xie, 2016, Triassic chrysophyte cyst fossils discovered in the Ordos Basin, China: Geology, v. 44, no. 12, p. 1031–1034, doi:10.1130/G38527.1.

Zhang, W., W. Yang, and L. Xie, 2017, Controls on organic matter accumulation in the Triassic Chang 7 lacustrine shale of the Ordos Basin, central China: International Journal of Coal Geology, v. 183, p. 38–51, doi:10.1016/j.coal.2017.09.015.

Zhao, J., N. P. Mountney, C. Liu, H. Qu, and J. Lin, 2015, Outcrop architecture of a fluvio-lacustrine succession: Upper Triassic Yanchang Formation, Ordos Basin China: Marine and Petroleum Geology, v. 68, Part A, p. 394–413.

Zhu, H., Y. Ju, M. Yang, C. Huang, H. Feng, P. Qiao, C. Ma, et al., 2022, Grain-scale petrographic evidence for distinguishing detrital and authigenic quartz in shale: How much of a role do they play for reservoir property and mechanical characteristic?: Energy, v. 239, Part C, 122176, 23 p., doi:10.1016/j.energy.2021.122176.

Zou, C., R. Zhu, Z. Chen, J. G. Ogg, S. Wu, D. Dong, Z. Qiu, et al., 2019, Organic-matter-rich shales of China: Earth-Science Reviews, v. 189, p. 51–78, doi:10.1016/j.earscirev.2018.12.002.